AGU PUBLICATIONS

JGR

Journal of Geophysical Research: Planets

RESEARCH ARTICLE
10.1002/2017JE005276

Key Points:
- The presence of diverse hydrated minerals in lowland craters is consistent with excavation of an aqueously altered ancient basement
- Widespread mafic minerals associated with impact craters indicate buried volcanic units with calculated volumes greater than prior estimates
- No strong evidence for widespread carbonate or evaporative salts has been found to support the hypothesis of a global ocean

Supporting Information:
- Supporting Information S1
- Data Set S1

Correspondence to:
L. Pan,
lpan@caltech.edu

Citation:
Pan, L., B. L. Ehlmann, J. Carter, and C. M. Ernst (2017), The stratigraphy and history of Mars' northern lowlands through mineralogy of impact craters: A comprehensive survey, *J. Geophys. Res. Planets*, *122*, 1824–1854, doi:10.1002/2017JE005276.

Received 25 JAN 2017
Accepted 10 AUG 2017
Accepted article online 16 AUG 2017
Published online 9 SEP 2017
Corrected 30 NOV 2017

This article was corrected on 30 NOV 2017. See the end of the full text for details.

The stratigraphy and history of Mars' northern lowlands through mineralogy of impact craters: A comprehensive survey

Lu Pan[1], Bethany L. Ehlmann[1,2], John Carter[3], and Carolyn M. Ernst[4]

[1]Division of Geological and Planetary Sciences, California Institute of Technology, Pasadena, California, USA, [2]Jet Propulsion Laboratory, California Institute of Technology, Pasadena, California, USA, [3]Institut d'Astrophysique Spatiale, Orsay, France, [4]The John Hopkins University Applied Physics Laboratory, Laurel, Maryland, USA

Abstract The basin-filling materials of the northern lowlands, which cover approximately one third of Mars' surface, record the long-term evolution of Mars' geology and climate. The buried stratigraphy was inferred through analyses of impact crater mineralogy, detected using data acquired by the Compact Reconnaissance Imaging Spectrometer for Mars. Examining 1045 impact craters across the northern lowlands, we find widespread olivine and pyroxene and diverse hydrated/hydroxylated minerals, including Fe/Mg smectite, chlorite, prehnite, and hydrated silica. The distribution of mafic minerals is consistent with infilling volcanic materials across the entire lowlands (~1–4 × 10^7 km^3), indicating a significant volume of volatile release by volcanic outgassing. Hydrated/hydroxylated minerals are detected more frequently in large craters, consistent with the scenario that the hydrated minerals are being excavated from deep basement rocks, beneath 1–2 km thick mafic lava flows or volcaniclastic materials. The prevalences of different types of hydrated minerals are similar to statistics from the southern highlands. No evidence of concentrated salt deposits has been found, which would indicate a long-lived global ocean. We also find significant geographical variations of local mineralogy and stratigraphy in different basins (geological provinces), independent of dust cover. For example, many hydrated and mafic minerals are newly discovered within the polar Scandia region (>60°N), and Chryse Planitia has more mafic mineral detections than other basins, possibly due to a previously unrecognized volcanic source.

Plain Language Summary The northern lowlands of Mars (encompassing one third of the planet's surface area) could have hosted a global ocean in the past. The lowlands are composed of several topographic depressions ("basins") filled with sediments, which mask the nature of the underlying crust. Impact craters excavate up to several kilometers into the subsurface of the lowlands and expose the hidden record of its geologic history. Our comprehensive survey of the subsurface mineralogy excavated by these impact craters reveals widespread volcanic and hydrated silicate minerals. We did not find widespread carbonate, chloride, or sulfate salts, which would have suggested a long-lived global ocean. However, our observations do suggest that impact craters have excavated a crust made of 1 to 2 km of volcanic material, which is on top of a water-altered basement containing hydrated silicate minerals. We have also discovered local variations in the different basins with evidence for new volcanic sources and for hydrated minerals in ancient crust near the north polar cap.

1. Introduction

The northern lowlands of Mars preserve a long-term record of Mars' geologic history, including heavily cratered Noachian basement [*Frey et al.*, 2002], Hesperian outflow channels and/or possible ocean deposits [*Tanaka et al.*, 2003; *Parker et al.*, 1993], widespread Hesperian lava flows [*Head and Kreslavsky*, 2002], and Amazonian surface sedimentary/volcanic geomorphic structures (cones, knobs, polygons, etc.) [*Frey et al.*, 1979; *Lucchitta et al.*, 1986; *Farrand et al.*, 2005; *Oehler and Allen*, 2012]. The surface of the northern lowlands is covered by geologic units dated from the Early Hesperian to the Amazonian and has been mapped in great detail [*Tanaka et al.*, 2005, 2014]. However, little is known about the stratigraphic relationships between the underlying cratered basement, widespread lava flows, and subsequent units, including their thicknesses and variability across the northern lowlands. Questions also remain regarding the spatial and temporal variations of aqueous activity in the northern lowlands and the possible existence of an ancient global ocean. Study of

the subsurface stratigraphy of the northern lowlands thus presents an opportunity to assess past Martian igneous and aqueous processes changing through time.

Our ability to interpret the mineralogy of the subsurface of the northern lowlands has been limited by mantling deposits and coatings that obscure the composition of surface units as well as limited exposure of underlying units. Few tectonic scarps exist that would expose materials in section. Instead, impact craters that excavate bedrock provide the key means of accessing the subsurface stratigraphy of the northern lowlands. In this study, we apply a set of improved noise reduction tools to analyze data acquired by the Compact Reconnaissance Imaging Spectrometer for Mars (CRISM) onboard the Mars Reconnaissance Orbiter (MRO). We analyze high spatial resolution, targeted data covering part or all of 1045 impact craters in the northern lowlands to assess the mineralogy of their units, which includes materials excavated from the subsurface. From the frequency and geologic context of different types of mineral-bearing units, we consider the implications for the subsurface stratigraphy and provide insights into the geologic and aqueous history of the northern lowlands of Mars.

In this paper we first review existing knowledge about the northern lowlands (section 2); describe the CRISM processing methods and crater data set used in this study (section 3); present the results of mineral detections, spatial distribution, and statistical relationships with crater size and other key variables (section 4); discuss the implications for the geologic history of the northern lowlands, including igneous and aqueous activity (section 5); and summarize key conclusions (section 6).

2. History and Composition of the Northern Lowlands

The northern lowlands, also known as the northern plains, are divided from the southern highlands by the crustal dichotomy boundary, which has long been recognized and hypothesized to have formed early in Mars' history due to a large impact [*Marinova et al*., 2008; *Andrews-Hanna et al*., 2008], several impacts [*Frey*, 2006], or mantle convection [*Zhong and Zuber*, 2001]. Topography data from Mars Orbiter Laser Altimeter (MOLA) and gravity data from Doppler tracking on Mars Global Surveyor show that the northern lowlands have an average elevation approximately 5 km lower than the cratered southern highlands and a much thinner crust (30–40 km) than that of the highlands (70–80 km) [*Smith et al*., 1999; *Zuber et al*., 2000]. Due to its unique geologic history, the northern lowlands are also distinctive from the southern highlands of Mars with its smoother surface and younger age [*Aharonson et al*., 1998; *Tanaka et al*., 2005, 2014] as well as a different surface composition (described below).

The smoothness and low crater density indicate a surface of Late Hesperian-Amazonian age over the majority of the lowlands [*Tanaka et al*., 2005, 2014]. However, subtle circular depressions called Quasi Circular Depressions have been identified in MOLA data throughout the lowlands [*Frey et al*., 2002; *Frey*, 2008], probably indicating a heavily cratered Noachian or pre-Noachian surface buried underneath plains materials. Also, the topographic expression of wrinkle ridges is consistent with widespread Hesperian lava flows that may account for most of the post-Noachian fill within the northern basin [*Head and Kreslavsky*, 2002], a scenario that may have had significant influence on Mars climate due to the release of volatiles as part of the volcanic eruptions. Due to the lack of good exposures in the plains, there are uncertainties regarding the relationship between the ancient basement and widespread lava flows indicated by wrinkle ridges, including whether intermediate stratigraphic units exist between the two. The composition and depth of this ancient basement may hold important clues to understanding the nature of the dichotomy, and a detailed analysis of the thickness of the surface lava unit(s) may provide better constraints for the volume of volcanic deposits in the northern lowlands.

Two proposed shorelines that follow topographic contours suggest the possible past existence of ocean(s) in the Noachian [*Clifford and Parker*, 2001] or Early Hesperian [*Carr and Head*, 2003]. Evidence for shoreline features has been challenged because later mapping shows the contacts do not follow equipotential surfaces [*Malin and Edgett*, 1999; *Carr and Head*, 2003], though these observations may be reconciled with other mechanisms like true polar wander [*Perron et al*., 2007]. Later, the identification of 29 fan deposits, purported to be deltas, within a 200 m topographic contour near the dichotomy was also used to suggest a past ocean [*Di Achille and Hynek*, 2010]. Regardless of whether an ocean existed for long periods of time, large outflow channels certainly repeatedly debouched into the plains in the Hesperian and early Amazonian, presumably depositing large quantities of sediments [*Tanaka*, 1997; *Tanaka et al*., 2001]. Widespread aqueous alteration

might occur given the existence of repeated outflow deposits or an ocean, which may leave evidence in sedimentary deposits in the stratigraphic record [e.g., *Salvatore and Christensen*, 2014b]. The evaporation of a large standing body of water could also precipitate carbonate and other salts in localized, if not extensive, regions as the topmost aqueous deposits in the stratigraphy. These minerals, previously unidentified in the northern lowlands, may lie deep beneath the current northern lowlands surface, so the investigation of the underlying mineralogy would add an important line of evidence to the existence/absence of an ancient global ocean.

Other sedimentary processes (e.g., aeolian and periglacial) have also been observed within the northern lowlands. The Vastitas Borealis Formation (VBF), a widespread sedimentary unit on the surface of the northern lowlands, probably represents one of the final stages of water-related sedimentary activity. The VBF has been suggested to have resulted from either volatile expulsion from the compaction of a fluid-laden sedimentary unit [*Salvatore and Christensen*, 2014b], local periglacial processes acting on outflow channel sediments and other older plain materials [*Tanaka et al*., 2003], sublimation residues [*Kreslavsky and Head*, 2002], or ocean sediments [*Parker et al*., 1989, 1993; *Baker et al*., 1991]. On the surface of the Vastitas Borealis Formation many geomorphic features that could be related to aqueous activity have been identified, including polygonal troughs for ice/volatile-related processes [*McGill and Hills*., 1992; *Hiesinger and Head*, 2000; *Yoshikawa*, 2003; *Mangold et al.*, 2004] and conical and domical features hypothesized to be mud volcanoes or springs [*Farrand et al.*, 2005; *Oehler and Allen*, 2010]. Any hydrated/hydroxylated mineral associated with the unit may help to distinguish the different formation mechanisms for the Vastitas Borealis Formation.

The subsurface mineralogy of the northern lowlands may also be unevenly distributed among geographically separated basins, which have been subject to local sedimentary and volcanic resurfacing in addition to any lowland-wide processes. For example, outflow channel sediments may have been deposited in Chryse and Acidalia Planitiae [*Tanaka et al*., 2001; *Salvatore and Christensen*, 2014a]; continuous activity of Elysium Mons volcanic province has filled much of Elysium and Utopia Planitiae [*Hartmann and Berman*, 2000; *Platz and Michael*, 2011]; and Arcadia and Amazonian Planitiae have been resurfaced with extensive volcanic flows probably sourced from Olympus Mons [*Fuller and Head*, 2002]. The detailed basin-specific stratigraphy and resurfacing processes also constitute major components of the geology of the northern lowlands and will be investigated in this study.

Previous works on compositional data in the northern lowlands provide important understanding of their geologic history. Thermal infrared data acquired from Thermal Emission Spectrometer (TES) indicate a relatively silica-enriched surface (surface type II) compared to the typical basalt (Surface type I) of the southern highlands [*Christensen et al*., 2001]. Therefore, the surface of the lowlands was initially interpreted to be andesitic in composition [*Bandfield et al*., 2000] but later reinterpreted to represent altered terrains [e.g., *Wyatt and McSween*, 2002; *Kraft et al*., 2003; *Michalski et al*., 2005]. Gamma Ray Spectrometer data do not show enhancement of Si in the bulk rock [*Karunatillake et al*., 2006; *Boynton et al*., 2007], thus favoring the interpretation that spectral differences may be explained by the presence of a thin silica-enriched coating or rind [e.g., *Kraft et al*., 2003]. Later, visible/shortwave-infrared (VSWIR) imaging spectrometers (e.g., OMEGA (Observatoire pour le Mineralogie, l'Eau, la Glace et l'Activité) and CRISM) showed much of the surface of the northern lowlands that has a characteristic downward slope toward longer wavelengths (the "blue" slope) [*Mustard et al*., 2005]. The distinct spectral features relative to the southern highlands may be due to dust cover, silica-enriched coatings, and/or a weathered glass [*Ruff and Christensen*, 2002; *Kraft et al*., 2003; *Mustard et al*., 2005; *Horgan and Bell*, 2012].

Higher spatial resolution studies of composition have shown that the mineralogy of the northern lowlands is not completely obscured. Mesas at the margins of the dichotomy boundary and the surfaces of intervening terrains show diverse hydrated silicates, including plateaus with Fe/Mg phyllosilicates and silica in stratigraphically higher but often topographically lower units [*Pan and Ehlmann*, 2014]. Also using CRISM data, mafic minerals were identified in 182 craters (0.3–62.7 km in diameter) in Acidalia Planitia [*Salvatore et al*., 2010], olivine was detected in multiple northern lowlands locales [*Ody et al*., 2013], and hydrated minerals were found in 9 large northern lowlands craters (20–230 km in diameter) [*Carter et al*., 2010]. As previous work suggested [*Head and Kreslavsky*, 2002], the mafic detections were interpreted to indicate the excavation of materials formed during widespread volcanism [*Salvatore et al*., 2010; *Ody et al*., 2013]. Hydrated minerals were interpreted to result from the excavation of altered Noachian crustal materials [*Carter et al*., 2010]. Additional occurrences of hydrated minerals associated with impact craters and other morphological

features (e.g., cones and polygonal troughs) were found in a global survey by *Carter et al*. [2013a], but their geologic context has not yet been examined in detail.

To gain a more complete and detailed understanding of the geologic history of the northern lowlands as indicated by compositionally distinct units, we surveyed all the CRISM images associated with impact craters in the northern lowlands. This work builds on previous successful surveys of the mineralogy of crater central peaks mostly in the southern highlands using near-infrared data [*Sun and Milliken*, 2015; *Caudill et al*., 2012; *Quantin et al*., 2012]. Impact craters can excavate subsurface materials and expose them within the crater central peak/ring structure, crater walls, ejecta blanket, and on the crater floor, making it possible for us to access the subsurface stratigraphy to varying degrees using orbital data. Craters of different sizes may expose distinctive mineralogy in the ejecta and reveal the depths of subsurface units by physical constraints on the maximum excavation depth [e.g., *Budney and Lucey*, 1998; *Baratoux et al*., 2007; *Ernst et al*., 2010; *Barnhart and Nimmo*, 2011]. Central peaks of large complex craters sometimes expose the deepest stratigraphy brought to the surface by the impact [e.g., *Ernst et al*., 2010]. Inverted flaps exposed on the crater walls access the shallow subsurface [e.g., *Salvatore et al*., 2010; *Salvatore and Christensen*, 2014b]. Impact craters into volatile-rich substrates can also initiate long-lived hydrothermal systems, if sufficient water/ice and heat are available [e.g., *Rathbun and Squyres*, 2002; *Abramov and Kring*, 2005; *Schwenzer et al*., 2012]. Thus, the geologic context of hydrated mineral detections must be examined to understand their origins. Through analyses of the origins of detected minerals in craters and their association with impact crater size and morphology, we will be able to construct basic stratigraphies, constrain scenarios for lowland-wide evolution, discover region-specific geology that was previously unknown, and unravel the buried record of geologic and aqueous activity within the northern lowlands of Mars.

3. Data and Method

3.1. Study Region and CRISM Coverage

To better understand the stratigraphic framework of the northern lowlands, we focus on the analysis of spectral data from the CRISM instrument onboard MRO, acquired at the instrument's highest spatial sampling. CRISM L-detector targeted images cover the wavelength region from 1 μm to 3.92 μm, which includes electronic transitions of Fe and vibrational absorptions related to OH, H_2O, CO_3, SO_4, and metal-OH. CRISM targeted images cover approximately 10 km wide areas with a spatial resolution of 15–19 m/pixel for full resolution images (FRT and FRS) and ~36 m/pixel for half-resolution images (HRL and HRS) [*Murchie et al*., 2009]. Here we adapt and improve an enhanced noise reduction algorithm (see section 3.2) to examine all the CRISM targeted images in the northern lowlands over any part of an impact crater, including the central structure, crater walls, crater floor, and ejecta blanket. For the purpose of this work, we study all identified impact craters with diameters ≥1 km in the northern lowlands with coverage of CRISM targeted L-detector data as of November 2015. We focus on the well-calibrated 1.0–2.6 μm channels from the L-detector because both mafic and hydrated minerals are expressed in the spectral range; in locations with hydrated mineral detections, we examined select S-detector data (covering 0.4–1.0 μm) to search for crystalline iron oxides but did not find them. The region of interest is shown in Figure 1, with the outline of the study region bounded by contour lines along the dichotomy boundary, following *Tanaka et al*. [2005] and excluding the northern polar cap. A total of 18,293 impact craters ranging in diameter from 1 km to 376 km lie within the proposed study region, documented in Mars' global crater database [*Robbins and Hynek*, 2012]. Among these, 1045 craters are covered by 2257 CRISM targeted images. The craters are distributed across the northern lowlands from the equator to ~80°N with some biases in targeting (Figure 1). Denser CRISM coverage exists closer to the pole due to the higher repeat rate of observations in MRO's polar orbit. CRISM coverage may vary significantly for different craters since more targets are placed after minerals are detected with CRISM or OMEGA.

3.2. CRISM Processing Using a Noise Reduction Algorithm

To fully utilize the CRISM data set in the northern lowlands of Mars, an improved CRISM noise reduction tool has been implemented to facilitate mineral detection, adapted from a previous automated processing pipeline [*Carter et al*., 2013b], using a subset of routines. The detailed workflow is described below (Figure 2):

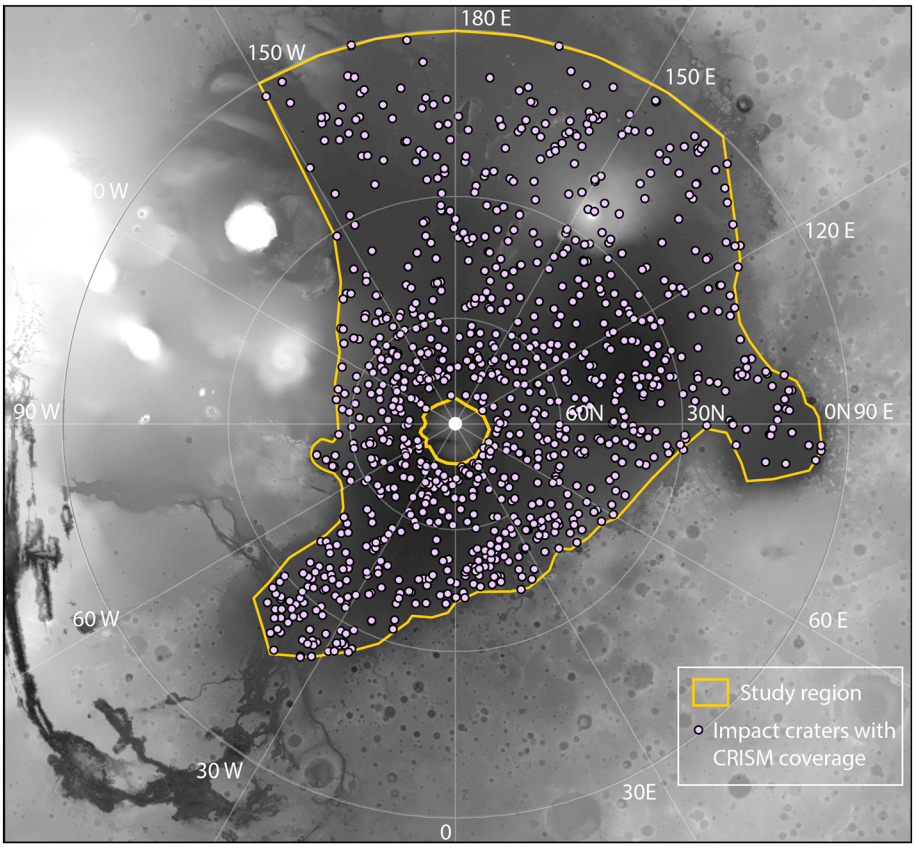

Figure 1. Study region of this investigation, which includes the area encompassed by the boundary of the dichotomy between the northern lowlands and the southern highlands, excluding the northern polar cap (orange line). The purple dots indicate impact craters with CRISM coverage that meet the requirements of this work: (a) With crater diameter over 1 km; (b) located within the study region (outlined here); (c) with CRISM L-detector data over any part of the crater, including central structure, rim, floor, and ejecta. The base map is Mars topography data from Mars Orbiter Laser Altimeter (MOLA) in Mars North Polar Stereographic Projection.

1. First, CRISM I/F files are downloaded from the Planetary Data System, and we use standard data processing procedures to perform atmospheric correction using the volcano-scan method [*Mustard et al.*, 2005] and photometric correction through the CRISM Analysis Toolkit (CAT).
2. Then based on the atmospherically and photometrically corrected data cube, we find statistical outliers in spectral dimension in a given image, which are possibly due to the anomalous behavior of the detector (criteria: single channel offset $>$1.5% of predicted value based on the boxcar average of adjacent 10 channels). We then replace the spurious value with the predicted value from a boxcar average of 30 adjacent channels in the spectral domain. This limits the effect of spectral spikes for later processing. This selection threshold is set so that only features with unreasonable reflectance values and single-channel spikes are selected so as to avoid overcorrecting for spectral absorption features. The product of these steps is the "corrected I/F cube" product (Figure 3.1).
3. Afterward, several spectral parameters characteristic of particular mineral spectral features are

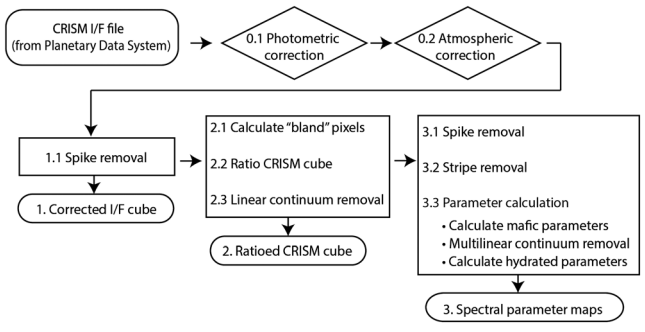

Figure 2. Flow chart and products of the preprocessing algorithm for CRISM data to reduce noise and highlight mineral detections.

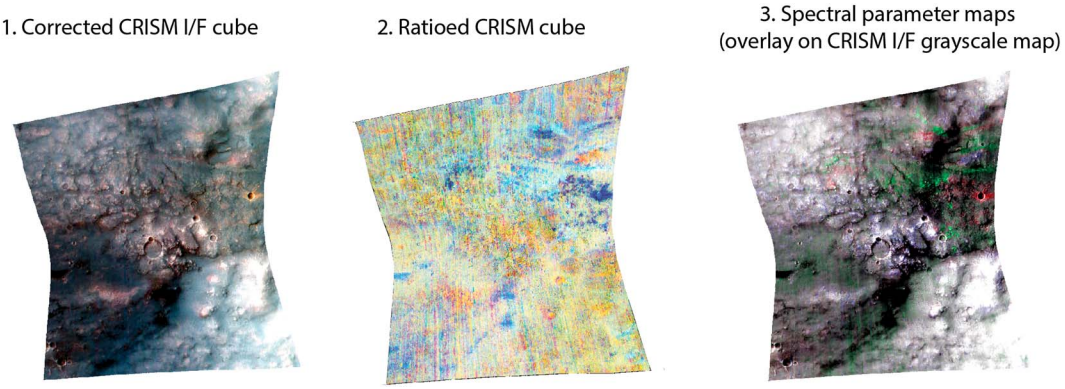

Figure 3. Data products from preprocessing algorithm for a CRISM full resolution target IR image (FRT00018AEF_07_IF167L_TRR3) as sample data product from noise processing.

computed (after *Pelkey et al*. [2007] and *Carter et al*. [2013b]). Then, instead of the conventional method of handpicking in-scene denominator spectra to calculate spectral ratios for areas with strong parameter values, an algorithm automatically identifies the pixels within the same image below a threshold value (median + 1.5σ) for several spectral parameters (as benchmarked in *Carter et al*. [2013b]). We then create column-specific "bland" spectra for the scene using the median of the selected pixels in each column. For columns with no "bland" pixel, the median spectrum of the entire column is used as the denominator. This step removes most instrument artifacts and atmospheric residuals. After computing scene-derived denominator spectra, this algorithm calculates the ratio of the entire scene, which accentuates all the possible mineral detections relative to the spectrally bland regions in the same image. Each pixel in the scene is then normalized to a linear continuum based on the corrected I/F values at 1.76 and 2.14 μm, wavelengths chosen because few minerals relevant to Mars have absorptions at these wavelengths. With this normalization and continuum removal method, the effect of reflectance and illumination geometry on the spectral ratio is minimized in the "ratioed CRISM cube" (Figure 3.2), which is used for the quick identification of spectra of regions of interest.

4. To produce an improved parameter map, using more aggressive noise filtering that could influence spectral shape, we first apply empirical methods of additional despiking and destriping to the ratioed CRISM cube. As in the previous despiking step, we find statistical outliers in the spectral dimension and replace with the value of with a 30-channel boxcar average in the spectral domain (criteria: single channel offset over 1% of predicted reflectance value based on 10 channel average). We then calculate an average corrected I/F spectrum for each image column. The columns are normalized by the average value of the entire column (calculated as the mean of the median spectrum of the upper, middle, and lower one-third of the column) to remove the stripes in the along-track direction.
5. Then, spectral parameters are calculated to emphasize the band depth (*bd*) of different wavelengths based on I/F value of the band of interest (R_{band}) and the calculated I/F value of the continuum ($R_{\text{continuum}}$):

$$bd = 1 - \frac{R_{\text{band}}}{R_{\text{continuum}}} \tag{1}$$

[*Clark and Roush*, 1984].

The band depths of absorption features of typical minerals previously found on Mars are calculated with band centers chosen to represent different chemistries in hydrated minerals (e.g., 2.29 μm for Fe-smectite; 2.31 μm for Mg phyllosilicate; 2.21 μm for Al-phyllosilicate). For hydrated minerals, instead of the usual spectral parameter maps calculated directly from the I/F cube [e.g., *Viviano-Beck et al.*, 2014], we compute and examine the band depth map using the despiked and destriped ratioed CRISM cube because absorption features for hydrated minerals are accentuated and isolated from overall continuum effects (Figure 3.3). The result, the new "spectral parameter map" (Figure 3.3), is used to aid the quick identification of mineral absorption features in a hyperspectral cube.

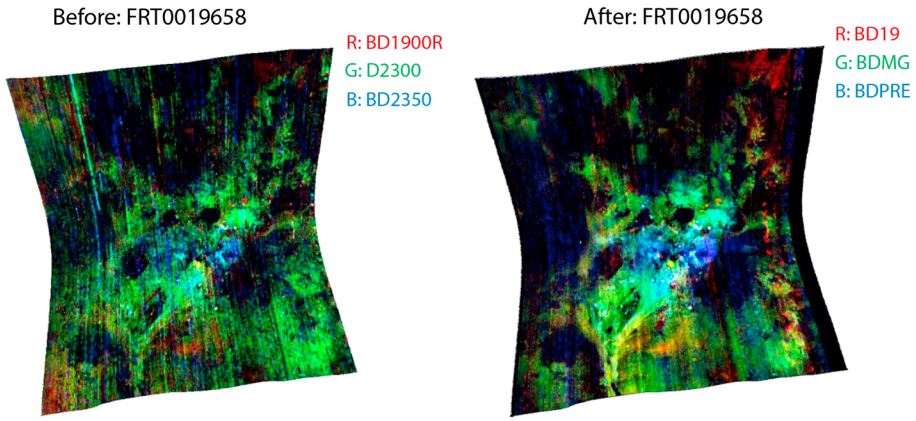

Figure 4. (right) Example denoised parameter map compared to a (left) parameter map calculated from a nonprocessed CRISM I/F image (FRT0019658) that was simply photometrically and atmospherically corrected using the CRISM Analysis Tool (CAT). The colors represent different spectral parameter outputs in CAT and noise reduction process (red, green, and blue bands represent absorption depths at 1.9, 2.3, and 2.35 μm, respectively, indicative of hydrated minerals, Fe/Mg phyllosilicates or carbonates, and prehnite or chlorite, respectively).

Our tests and previous benchmarks on the northern lowlands images show that the application of the algorithm was successful in reducing noise and providing more details in spectral parameter maps (Figure 4) to further aid geologic interpretation. Limitations are understood as a result of vetting with sample images. Potential issues observed with the algorithm include the following: (a) if two or more adjacent channels are behaving irregularly, they will not be corrected in the despike step, a conservative choice made so as to avoid altering bands due to real mineral absorption; (b) mafic absorption features can be inverted by the ratioing step in images where a mafic signature is ubiquitous; (c) absorptions present that are not considered a priori become part of the "bland" pixels used in the ratio denominator, and thus, the absorptions are weakened or removed in the ratio product. Therefore, when applying this algorithm, we use the heavily processed cubes only for parameter mapping to highlight areas of interest. The ratio cubes are used for fast evaluation of spectra and are then compared with the original I/F spectra for validation of detections. The denoising algorithm reduces noise in the spectral domain for the northern lowlands data set and enables fast identification of mineralogically interesting areas, subject to the limitations above. We use this processing in mineral identification.

3.3. Mineralogy Analyses

We recorded the detections of different mineral phases (including olivine, pyroxene, Fe/Mg phyllosilicates, hydrated silica, chlorite/prehnite, sulfate, some minor hydrated minerals, and unidentified hydrated minerals), according to their spectral characteristics and documented where they occur (central peak, crater walls, floor, or ejecta). These detections are based on reference to terrestrial spectral library [e.g., *Clark et al*., 2007] and prior CRISM works [e.g., *Bishop et al*., 2008; *Ehlmann et al*., 2009; *Roach et al*., 2010]. We also find a few hydrated materials with absorption combinations that do not belong to the above categories or do not have a good match in the spectral library (see section 4). Detections with absorption bands that are hardly distinguishable from the noise or less certain due to the effect of dust cover or coatings on the spectral continuum are noted as "maybe" detections. Minerals detected in dark dunes, which commonly occur on crater floors or within ejecta, are not counted because these are unrelated to the local stratigraphy and rocks influenced by impact. Deposits associated with morphology other than dunes on the crater floor and ejecta, which may include disrupted bedrock, ejected materials from the impact or postimpact sedimentary units, often have indistinguishable origins at CRISM resolution and are thus included in the survey for completeness. Craters north of 40–50°N are sometimes found with spectral features of H_2O ice or CO_2 ice, which may mask some of the bedrock mineralogy. Detections (or "maybe" detections) are reported when minerals are present. Nondetection does not, however, imply absence, so our detections signify a lower bound on the prevalence of mafic and hydrated minerals in the northern lowlands.

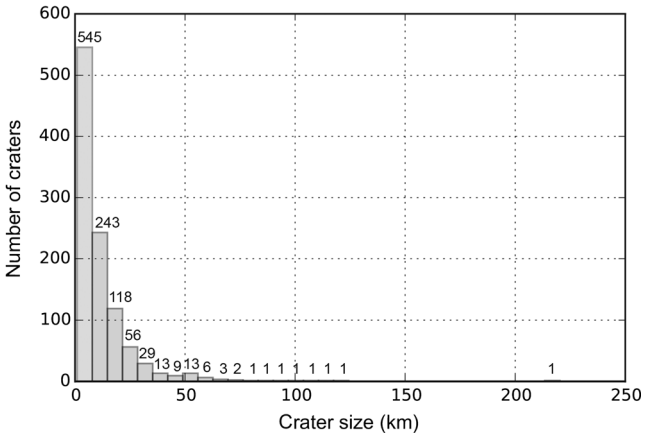

Figure 5. Size-frequency diagram for northern lowlands impact craters investigated in this study. The number of craters within each bin is labeled on the top of the bar.

3.4. Statistical Analyses of Crater Detection Results

To analyze the influence of crater size, dust cover, and modification, we fit a logistic regression function, $f(x)$, to the mafic and hydrated mineral detections in association with one or more crater morphology parameters (x) (e.g., crater diameter). For example, based on the ideal excavation model, small craters with excavation depths smaller than the minimum depth of the mineral-bearing strata (x_0) will not show detection of this mineralogy ($f(x) \sim 0$) while large craters will ($f(x) \sim 1$). The relationship can be expressed as

$$f(x) = \frac{1}{1 + e^{x - x_0}} \tag{2}$$

The significance of the fit shows the influence of crater diameter (or other morphologic parameters) on the outcome of mineral detection (sections 4.3.1 and 4.3.5).

We also delineate the northern lowlands into eight different geological provinces and perform statistical tests (using *Fisher's exact* test, *chi-square test* and *Mann-Whitney U* test) comparing frequencies of the mafic/hydrated mineral detections by geological province, which highlights regional differences in crater-associated mineralogy (section 4.3.2).

4. Results

4.1. Northern Lowlands Impact Crater Demographics and Mineral Occurrence Statistics

We analyzed 2257 images with CRISM L-detector data using the noise-reduction method, covering the central peak, crater wall, crater floor, and/or ejecta blanket of 1045 impact craters in the northern lowlands. The diameters of these impact craters range from 1 to 220 km (Figure 5). Mineral detections, categorized into mafic and hydrated minerals, are widespread in the northern lowlands, though there is considerable spatial variability in occurrence not solely related to image availability (Figure 6). Here an *occurrence* is defined as a geologic feature associated with a crater (e.g., wall, ejecta, and central peak) with a specific mineral detection in an image; e.g., several regions on the crater wall with the same mineralogy are documented as one occurrence, and each image may have more than one occurrence of each mineral, e.g., a hydrated mineral detection in both ejecta and central peak. In total, 251 craters (~24%) are found with 724 occurrences of mafic minerals and 81 craters (~8%) are found with 300 occurrences of hydrated minerals, including the probable detections with less certainty ("maybe" detections; section 3.3; Figures 6 and 7). Observed mineralogy varies with crater size. Both mafic minerals and hydrated minerals are identified in craters larger than 20 km distributed throughout the northern lowlands; for craters between 5 and 10 km and craters smaller than 5 km, mafic detections are still relatively widespread, while hydrated minerals are restricted to localized regions (Figure 6). In the following text, we discuss in detail the spectral characteristics and criteria for mineral detection, the distribution of each mineral, the correlation between crater size and mineralogy, the geographic distribution of mafic and hydrated materials throughout the northern lowlands, and other influencing factors including dust cover and crater modification.

4.2. Mineral Identifications and Spectral Characteristics

4.2.1. Mafic Minerals: Olivine and Pyroxene

Mafic minerals are widespread in 24% of craters of different sizes, including 585 occurrences of olivine in 246 craters and 139 occurrences of pyroxene in 69 craters (Figure 7). These minerals have been identified with processed CRISM L-data from absorptions due to electronic crystal field transitions of Fe [*Burns*, 1970].

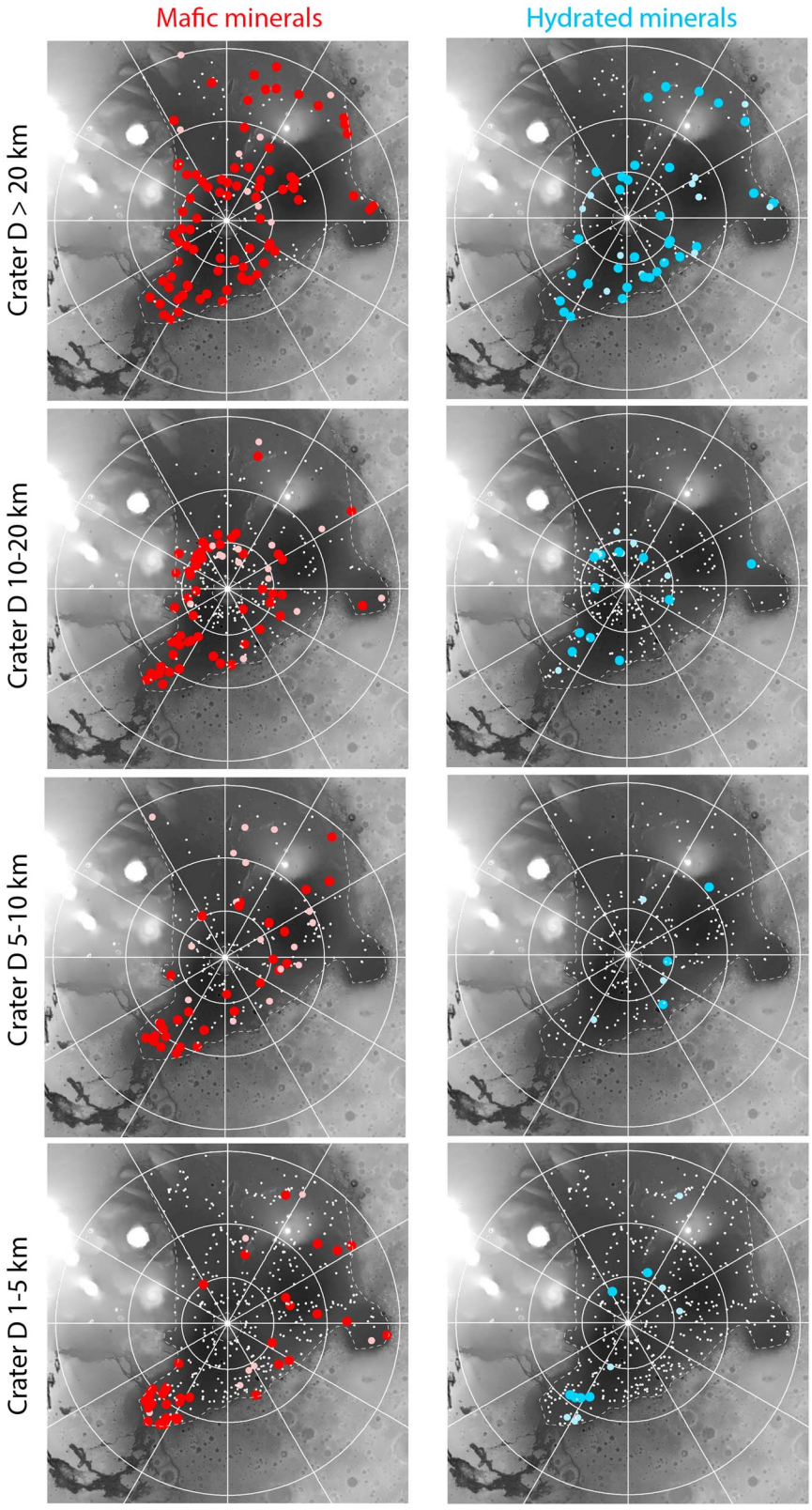

Figure 6. Distribution for all northern lowlands mafic and hydrated mineral detection binned by crater size. The lighter colored dots (pink, light blue) indicate craters where only absorption with less certainty ("maybe" detections) is found. The small white dots represent impact craters in the same size bin without detections. The maps showing the northern hemisphere with MOLA data as the base map in Mars North Polar Stereographic Projection.

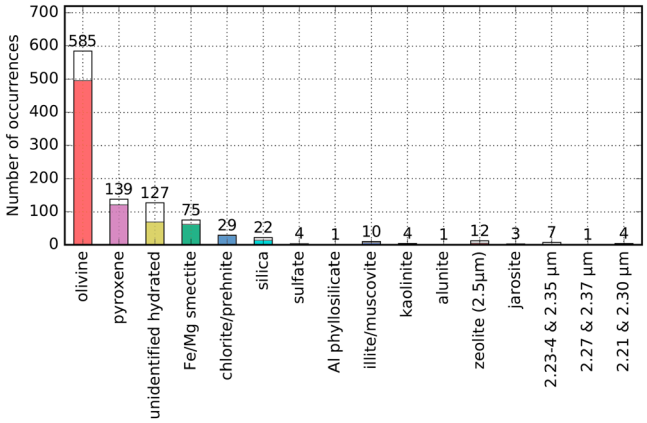

Figure 7. Histogram of major categories of mineral occurrences in northern lowlands impact craters (an occurrence counts for detection in a certain geological unit within a CRISM image). The white color represents detections that are probable but lack certain features ("maybe"). The total number of occurrences (including "maybe" detections) of each mineral or spectral class is given on top of the column.

Olivines ($(Mg, Fe)_2SiO_4$) have a broad absorption centered at 1 μm that varies according to Fe content (Figure 4a) [*Burns*, 1970]; *Sunshine and Pieters*, 1998]. Pyroxenes ($(Ca, Fe, Mg)_2Si_2O_6$) are identified by two broad absorptions around 1 and 2 μm, where the band centers shift to longer wavelengths with increasing calcium and iron content (Figure 8) [*Hazen et al.*, 1978; *Klima et al.*, 2007; *Klima et al.*, 2011]. Only detections with the presence of strong Fe absorption features and the absence of other vibrational features from hydrated minerals are counted in the mafic mineral category. Also, because typical Mars materials are basaltic and have mafic minerals, only units with enhanced olivine and pyroxene absorptions relative to nearby materials are recorded. In this study, we do not distinguish the detailed chemistry of mafic minerals but rather focus on the geographic and depth distribution of the detections.

4.2.2. Hydrated/Hydroxylated Minerals

A wide range of hydrated/hydroxylated minerals has been identified in the survey in 8% of the craters (Figures 7 and 9). Fe/Mg phyllosilicates (likely smectites or mixed-layered clays; 75 occurrences found in 32% of all craters with any hydrated mineral occurrences), chlorite or prehnite (29 occurrences in 11% of the craters), and hydrated silica (22 occurrences in 17% of the craters) are the most abundant hydrated

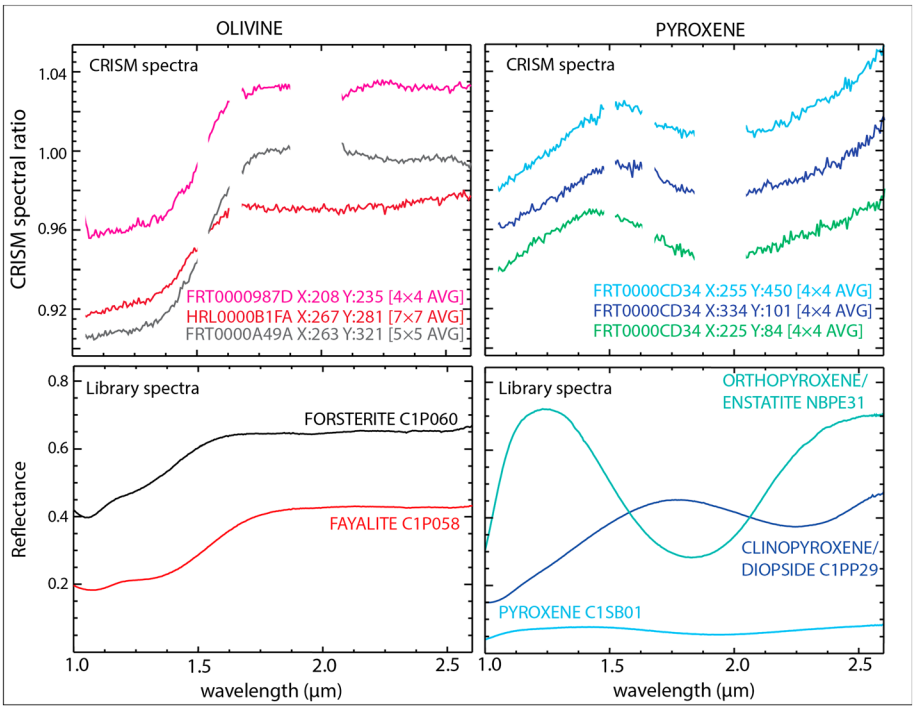

Figure 8. Laboratory reflectance spectra and CRISM ratioed spectra showing mafic minerals in the northern lowlands. (top row) Example spectra extracted from CRISM images in the northern lowlands; (bottom row) library spectra of olivine and pyroxene.

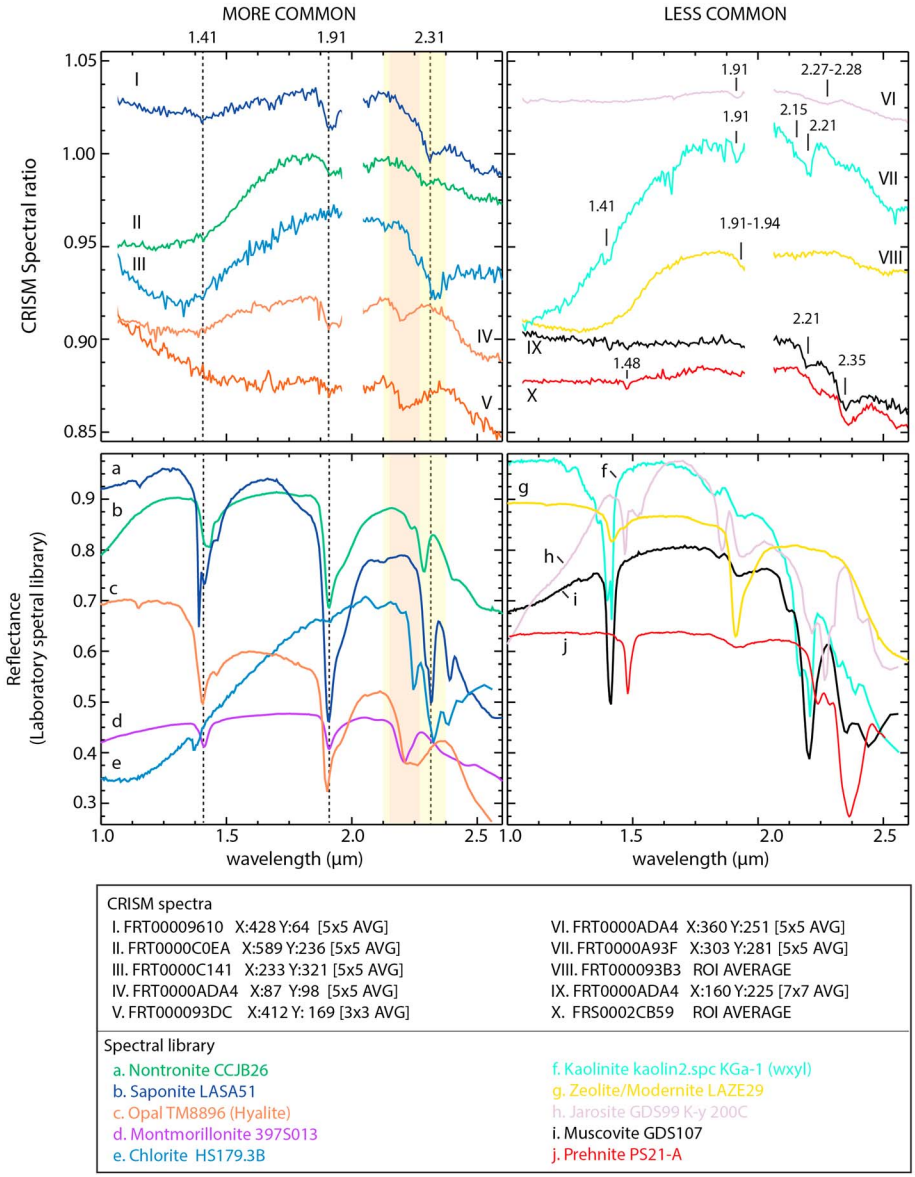

Figure 9. CRISM and laboratory reflectance spectra (from USGS spectral library [*Clark et al.*, 2007] and the CRISM spectral library) showing hydrated silicate mineral diversity in the northern lowlands. (top row) Example spectra extracted from CRISM images in the northern plains. (left) Fe/Mg phyllosilicates (I–II), chlorite (III), and hydrated silica (IV–V). The dashed lines are placed at 1.41, 1.91, and 2.31 μm. The shaded bars show the different 2.2 μm bandwidth in library spectra of montmorillonite and hydrated silica. (right) Detections of other (less common) hydrated minerals in the northern lowlands including the hydrated unidentified category. (bottom row) Library spectra of minerals with similar absorption features.

minerals that can be distinguished using spectral properties. Among the rest, kaolinite, illite, or muscovite, other Al-phyllosilicates and possible zeolites with a 2.5 μm absorption are found with 1–12 occurrences in 1–12% of craters but some of these detections with less certainty. Spectra with 1.9 μm absorption feature due to H_2O but lacking in other diagnostic absorptions constitute a significant fraction of mineral detections (with 127 occurrences). These are identified in 74% of all craters with any hydrated mineral detection and characterized as "unidentified hydrated" minerals. Each mineral class of detection is detailed below.

4.2.2.1. Fe/Mg Phyllosilicates

Fe/Mg phyllosilicates—we use the term to refer to smectites and mixed-layer clay minerals but not chlorite—are identified using 1.39–1.41, 1.91, and 2.29–2.31 μm absorptions due to H_2O overtones and combination modes as well as a Fe/Mg-OH stretching mode (Figure 9). For Fe/Mg smectites, the centers of absorption

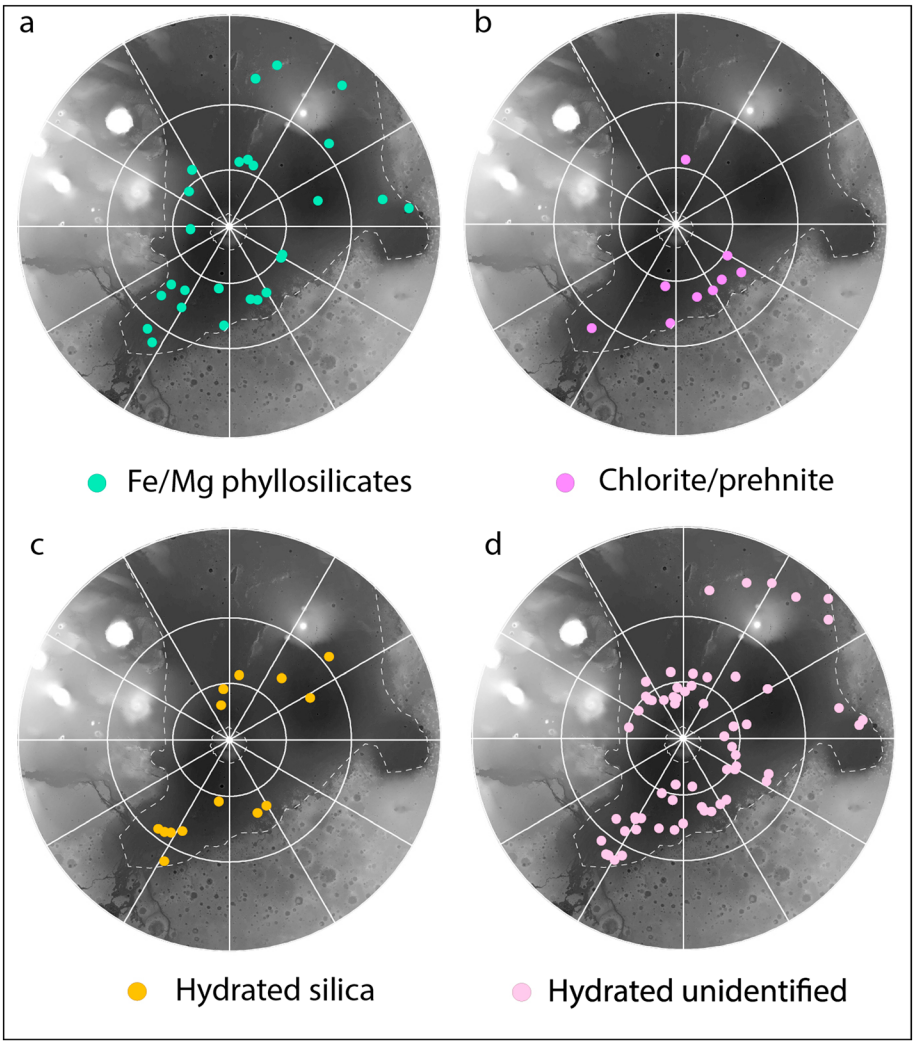

Figure 10. Northern lowlands hydrated mineral detection map for (a) Fe/Mg phyllosilicates (exclusive of chlorite), (b) chlorite/prehnite, (c) hydrated silica, and (d) unidentified hydrated minerals. Each dot represents a location of the center of an impact crater with at least one mineral detection. The base maps show the MOLA topography data of the northern hemisphere in Mars North Polar Stereographic Projection.

features shift due to variation in Fe or Mg as cations in the phyllosilicates: 1.41 and 2.31 μm for Mg-OH and 1.39 and 2.28–2.29 μm for Fe-OH absorptions [*Clark*, 1999; *Bishop et al*., 2002], sometimes accompanied by weaker 2.4 and 2.5 μm absorption features. In Martian spectra, some 1.41 μm absorption features are weak or absent, which could be a result of an alteration rind or coating.

As with other studies, we find that Fe/Mg phyllosilicates are the most abundant identifiable hydrated mineral [*Ehlmann et al*., 2011, *Carter et al*., 2013a]. In the northern lowlands, they are found in 75 occurrences in 26 impact craters with diameters ranging from 5.3 km to 220 km (Figure 10a). These phyllosilicates are found in all the major basins except Isidis Basin, where the CRISM coverage is less complete. Fe/Mg phyllosilicates in the northern lowlands show some variability in absorption band centers and shapes indicating variations in composition (Figure 9 spectra I and II).

4.2.2.2. Chlorite and Prehnite

Chlorite is a 2:1:1 phyllosilicate with a prominent 2.35 μm absorption due to Mg-OH combination tone and typically weaker or absent 1.9 μm absorption, sometimes accompanied by a 2.25–2.26 μm Al, Fe-OH or Al, Mg-OH stretching absorption [*Bishop et al*., 2008] (Figure 9 spectra III, e). It has distinctive spectral properties from other Fe/Mg phyllosilicates and thus can be discriminated. Prehnite is a Ca, Al-bearing inosilicate that is

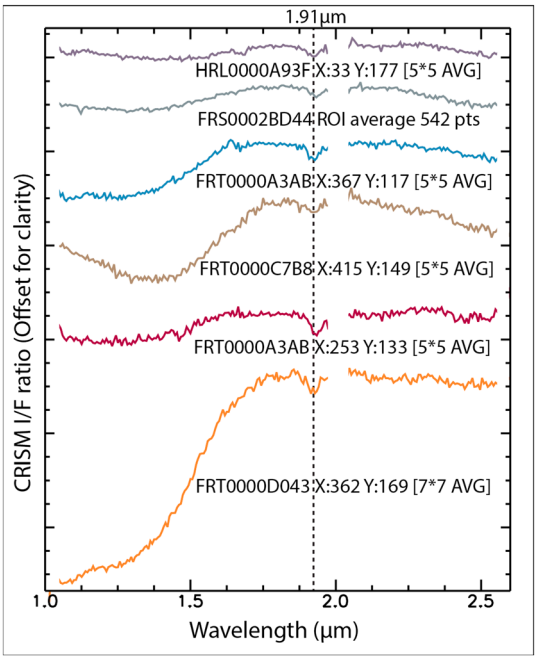

Figure 11. CRISM spectral ratio of unidentified hydrated minerals (labeled with CRISM image ID and the location/area of the region where spectra are taken from).

often associated with hydrothermal or low-grade metamorphic alteration on Earth. It is spectrally similar to chlorite, except with a sharp 1.48 μm absorption in addition to the 2.35 μm absorption. We found 29 occurrences with chlorite and/or prehnite detections in 9 northern lowlands craters (Figure 10b). The locations of these detections are limited to Chryse/Acidalia Planitiae, in the vicinity of Lyot crater (the largest fresh crater in the northern lowlands), and in Stokes crater. Chlorite/prehnite detections are often found to coexist with Fe/Mg smectites, and sometimes, they appear in mixture with Fe/Mg smectite and form a wider absorption from 2.31 to 2.35 μm as well as deeper 1.9 and 1.4 μm absorption features. Due to the spectral similarity with chlorite, prehnite may be present, but it is difficult to distinguish from chlorite with the quality of the orbital data and the concentration of the phases. In the northern lowlands, the additional 1.48 μm absorption clearly diagnostic of prehnite is observed in two occurrences, both on the outer rim of Lyot crater (as first reported in *Carter et al*. [2010]).

4.2.2.3. Hydrated Silica

Hydrated silica has been identified in 14 craters in the northern lowlands (Figure 10c). Hydrated silica is recognized with a broad absorption feature at 2.2 μm as well as 1.9 and 1.4 μm features. The broad feature at 2.2 μm is caused by two types of hydroxyl groups [*Anderson and Wickersheim*, 1964]. Different types of hydrated silica (including opal-A, opal-CT, opal-AG, cristobalite, and chalcedony) have varying relative strengths of 2.21 and 2.26 μm bands and slightly shifting band centers between 1.39 and 1.41 μm due to the relative amount of water and the bonding state of OH to Si in the mineral [*Milliken et al*., 2008; *Rice et al*., 2013; *Smith et al*., 2013]. Hydrated silica shares a similar spectral feature with Al-phyllosilicate (e.g., montmorillonite) in that both Al-OH and Si-OH vibrations cause absorptions around 2.21 μm. Hydrated silica, in general, has a wider absorption at 2.2 μm than Al-phyllosilicate (Figure 9V). However, in a few locations in the northern lowlands (including Stokes crater), the 2.2 μm absorptions are sometimes narrower than a typical 2.2 μm Si-OH absorption, yet wider than the Al-OH vibrational absorption (Figure 9IV).

Hydrated silica is less widespread than Fe/Mg phyllosilicates. They are found in relatively higher latitudes near Lyot crater, in Elysium Planitia, and in the Scandia region (e.g., reported previously in Stokes crater by *Sun and Milliken* [2015]), except for four clustered small craters in southern Acidalia Planitia (Figure 10c), with sizes ranging from 1 to 2.5 km. These hydrated silica detections are found on crater central peak, crater floor, crater walls, and ejecta blanket. Within the northern lowlands, there are also hydrated silica detections identified previously but not associated with craters: in the knobby terrains of Acidalia Planitia [*Pan and Ehlmann*, 2014] and in some of the cones and polygonal troughs in Utopia Planitia [*Carter et al*., 2013a]. These cases probably represent materials younger than the Fe/Mg phyllosilicates and may not be genetically related to the ancient basement that is excavated by craters.

4.2.2.4. Unidentified Hydrated Minerals

Another major category of hydrated mineral detections, in fact the most common category (found in 74% of all craters with any hydrated mineral occurrences), shows the 1.9 μm absorption, a combination tone of H_2O due to a vibrational absorption, but does not have distinguishable features from 2.1 to 2.5 μm and has been categorized as "unidentified hydrated" in the mineralogy survey (Figure 11). The absence of diagnostic

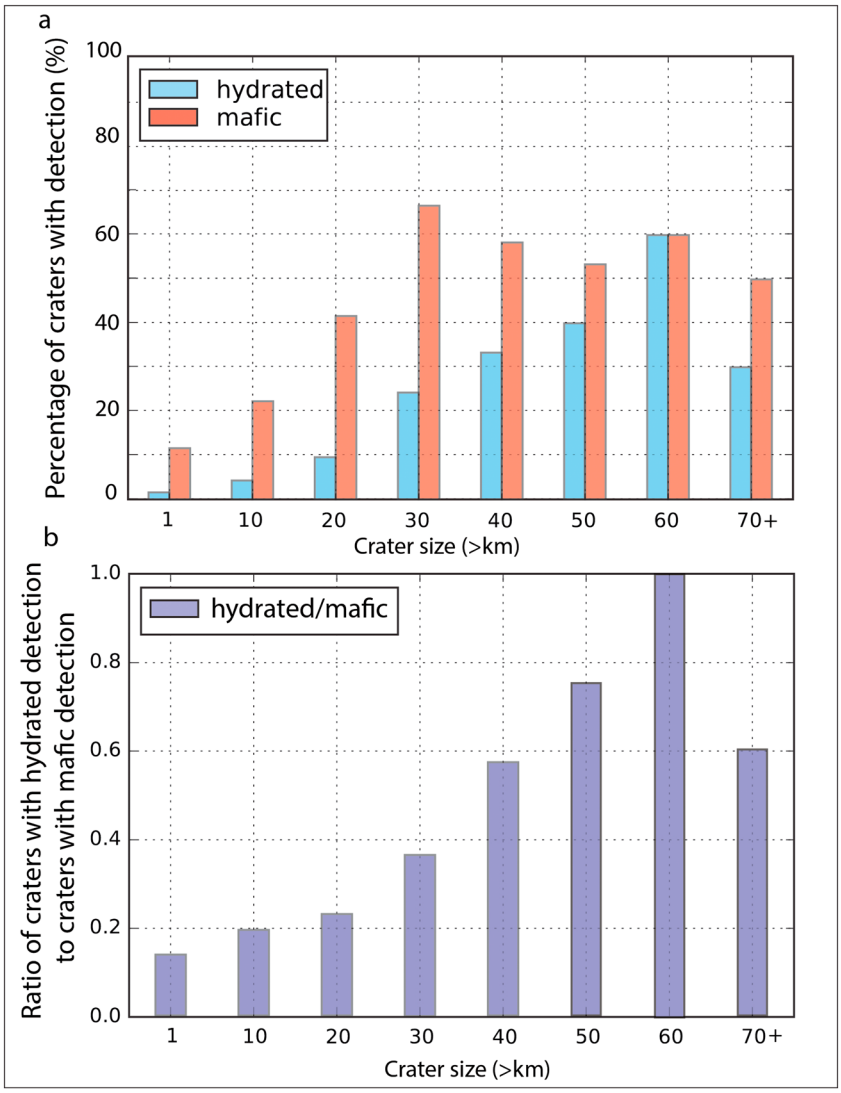

Figure 12. Histogram of impact crater mineral detections across the northern lowlands as a function of crater diameter. (a) The percentage of craters with mineral detections in binned crater sizes; (b) the ratio of craters with hydrated detections to mafic detections in binned crater sizes. Crater size is binned in intervals of 10 km diameter, and the bins are labeled based on the lower limit. Craters larger than 70 km are grouped into the last bin.

absorption features could be due to the nature of the materials, e.g., that they are hydrated salts or zeolites. In contrast to unidentified hydrated materials in the southern highlands, a 1.4 μm absorption, due to the first overtone of OH stretch or combination tones of H_2O, is not apparent in the northern lowland spectra. Observational factors such as surface coatings, dust mixing, low signal-to-noise ratio, and/or influence of aerosol or surface ice on CRISM spectra may confound detections of 1.4 or 2.1–2.5 μm absorptions, which are often weaker on Mars compared to laboratory spectra of terrestrial analogs. The spatial distribution of the unidentified hydrated minerals generally overlaps that of Fe/Mg phyllosilicates and does not show particular clustering in the northern lowlands (Figure 10d).

4.2.2.5. Minor Hydrated/Hydroxylated Species

There are other less common species found localized to a small number of craters within the northern lowlands. These spectra show absorption bands at 1.9 μm and between 2.1 and 2.5 μm. These spectra include possible Al-phyllosilicate with a 2.21 μm absorption, jarosite with a weak 2.27 μm absorption; illite or muscovite with absorption bands at 2.19–2.21 μm and 2.35 μm; kaolinite with a doublet at 2.15 and 2.21 μm; possible alunite with absorption at 2.17 μm; and possible zeolite detections with features at 2.5 μm, which may also be found in sulfate or carbonate (Figure 9). The small areas (small number of pixels) of these spectral

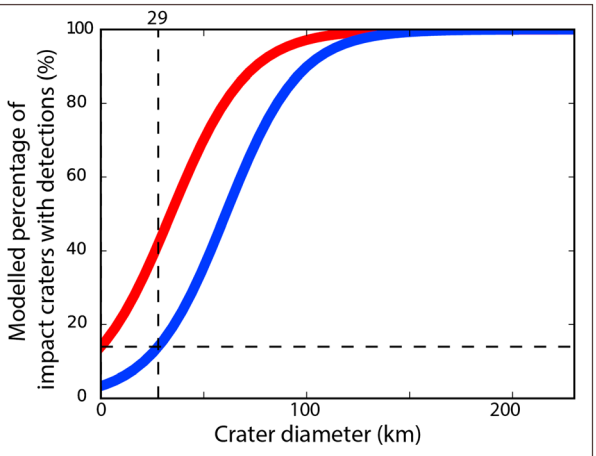

PROBABILITY OF DETECTION (X=DIAMETER)	MAFIC	HYDRATED
X = 0KM	0.15	0.04
X = 10KM	0.22	0.06
X = 20KM	0.32	0.09
X = 30KM	0.45	0.15
X = 50KM	0.58	0.24

Figure 13. Binary logistic function model for the probability of mafic and hydrated mineral detections as a function of crater diameter in the northern lowlands, based on the best fit logistic function of the observations. The table shows the predicted probability of detection for craters with different sizes in this model.

classes hinder our ability to make further distinctions, but these spectral classes indicate geographical variations and mineral diversity in some northern lowlands localities. For example, illite/muscovite detections are only found in multiple locations at Lyot and Stokes crater. Kaolinite has only one occurrence in Stokes crater (Table S1).

4.2.2.6. Mixtures of Hydrated/Hydroxylated Minerals

In some locations, additional bands at 2.19–2.21 μm, 2.26–2.27 μm, and 2.48–2.51 μm have been observed in addition to the 2.3 μm or 2.35 μm absorptions of Fe/Mg-OH. The combination of the spectral features cannot be matched to a specific mineralogy but may be caused by mixtures of different hydrated minerals. Three typical mixtures observed in the survey have absorption bands at 2.23–4 and 2.35 μm; 2.27 and 2.37 μm; and 2.21 and 2.31 μm. The combination of 2.23–4 and 2.35 μm absorptions closely resembles illite/muscovite detections but with wider and longer-wavelength absorption features around 2.23–4 μm than a typical illite/muscovite spectrum with 2.21 μm band, so the mixing of hydrated silica or Al-phyllosilicate with chlorite/prehnite is a more plausible explanation. The 2.27 and 2.37 μm absorption combination may be explained by a sulfate mineral possibly mixed with chlorite or prehnite. The combination of 2.21 and 2.31 μm does not have a good spectral match for a specific mineral either but can be explained by the coexistence of Al and Fe/Mg phyllosilicates. These mixtures are primarily found in Lyot crater and other smaller craters in its vicinity, Stokes crater, and one other crater east of Elysium Mons.

4.3. Crater Size, Geographical Distribution, and Other Influencing Factors for CRISM Detection

4.3.1. Mineral Detection Versus Crater Size

For craters smaller than 20 km in diameter, the percentage of craters found with at least one occurrence of hydrated/hydroxylated minerals is only 2%, as compared to 15% for mafic minerals. On the other hand, both hydrated minerals (~38%) and mafic minerals (~55%) are not uncommon for craters larger than 40 km (Figure 12a). In evaluating whether the difference in mineral detections is significant, effects of surface obscuration and differences in coverage can be accounted for, approximately, by ratioing the number of hydrated detections to mafic detections (Figure 12b). The increasing trend in the ratio of hydrated detections over mafic detections with increasing crater size implies that hydrated mineral detections are indeed more dependent on crater size.

The correlation between the percentage of craters with mineral occurrences and crater diameter (D) for both mafic and hydrated minerals can be fitted to a logistic function (see section 3.4) at a 99% confidence level. In the best fit logistic function (Figure 13), the fitted probability of detection is $p = 0.15$ for mafic mineral detection and $p = 0.03$ for hydrated mineral detection for the smallest crater size in the sample ($D = 1$ km). The probability of a hydrated mineral detection only reaches the same level ($p = 0.15$) for a crater size of 29 km. Both mafic and hydrated minerals have higher probability of occurrence in larger craters; however, compared to hydrated minerals, mafic detections are less dependent on crater size. The fact that hydrated minerals are more likely to be found in large craters can be explained by a deeper origin for hydrated minerals, by a scenario in which alteration occurred due to impact-induced hydrothermal activity, or a combination of the two (see section 5.2).

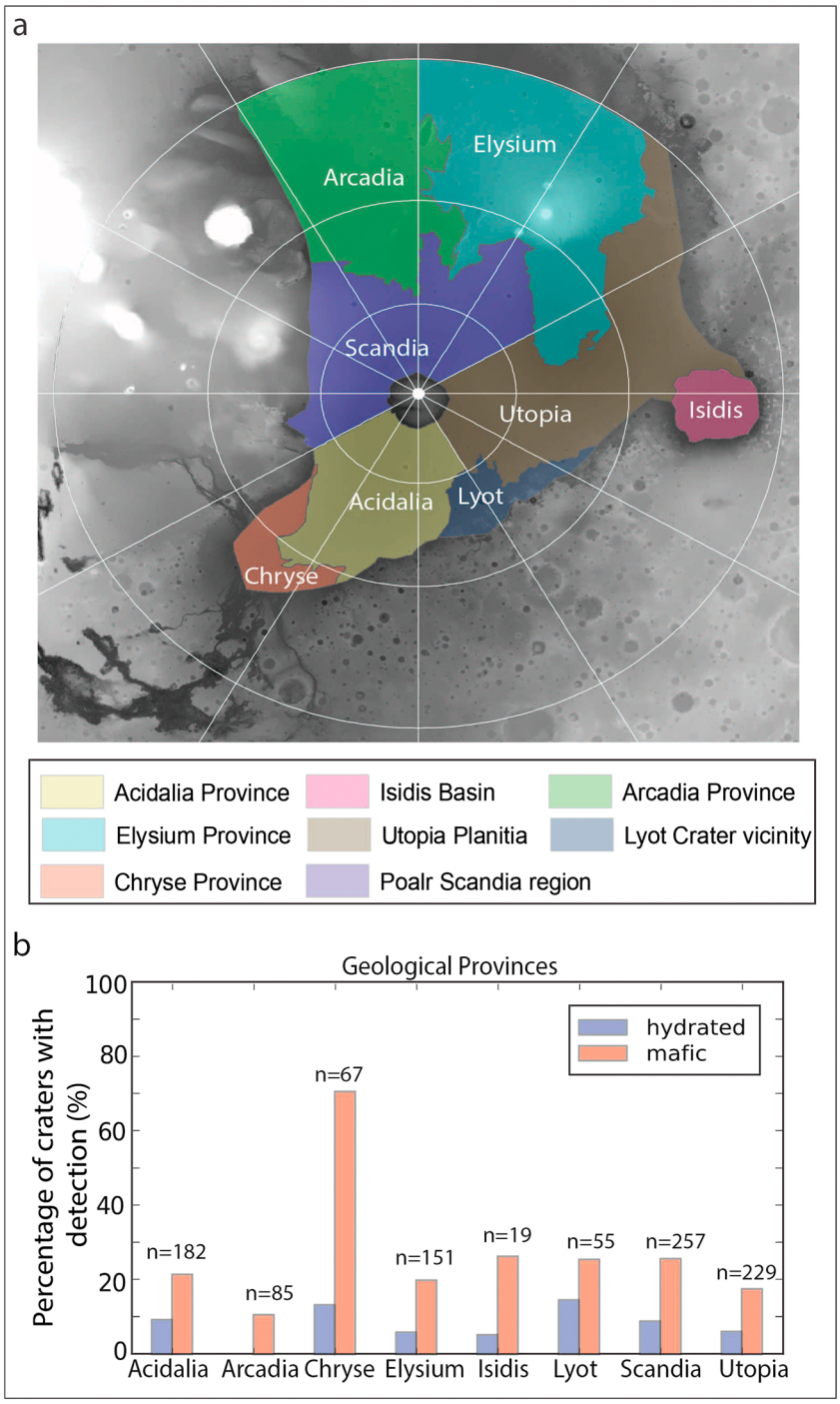

Figure 14. (a) Geological provinces in the northern lowlands delineated according to *Tanaka et al*. [2005]. (b) Comparison of different geological provinces on the percentage of craters with detection of mafic and hydrated minerals, with the total number of craters (*n*) in each geological province. The base maps are the MOLA topography data of the northern hemisphere in Mars North Polar Stereographic Projection.

4.3.2. Geographic Distribution of Mineralogy in the Northern Lowlands

To determine any region-specific processes and the related mineralogy, the northern lowlands were subdivided into eight major geologic provinces: Acidalia, Chryse, Lyot vicinity, Isidis, Utopia, Elysium, Arcadia, and Scandia region (Figure 14a). The geological boundaries follow previous geological mapping of the northern lowlands [*Tanaka et al*., 2005] with the "Borealis Province" subdivided into Acidalia, Utopia, and Scandia

Table 1. Statistical Tests (Fisher's exact Test, Chi-square test and Mann-Whitney U test) for Detections in Each Geological Province Compared to the Rest of the Northern Lowlands[a]

	Fisher's exact test		Chi square test		Mann-Whitney U test	
Mafic detections	Odds ratio	*p*-value	chi-square stat	*p*-value	U-stat	*p*-value
Acidalia (*n*=182)	0.8375	0.3916	0.6693	0.4133	76069.5	0.1842
Arcadia (*n*=85)	0.3513	0.0021*	8.4017	0.0037*	34835.0	0.0013*
Chryse (*n*=67)	9.6448	0.0000*	83.2607	0.0000*	16091.5	0.0000*
Elysium (*n*=151)	0.7550	0.2172	1.4261	0.2324	64221.5	0.0985
Isidis (*n*=19)	1.1324	0.7889	0.0549	0.8147	9519.0	0.4068
Lyot (*n*=55)	1.0849	0.7486	0.0621	0.8032	26812.5	0.3991
Scandia (*n*=257)	1.1263	0.5013	0.3889	0.5329	99026.5	0.2365
Utopia (*n*=229)	0.6068	0.0086*	5.3865	0.0203*	85592.5	0.0043*
Hydrated detections	Odds ratio	*p*-value	chi square stat	*p*-value	u-stat	*p*-value
Acidalia (*n*=182)	1.2863	0.3626	0.6430	0.4226	77021.5	0.1890
Arcadia (*n*=85)	0.0000	0.0012*	933.7471	0.0000*	37357.5	0.0027*
Chryse (*n*=67)	1.9526	0.0929†	3.0248	0.0820†	30774.0	0.0362*
Elysium (*n*=151)	0.7236	0.5094	0.6773	0.4105	66084.0	0.1870
Isidis (*n*=19)	0.6569	1.0000	0.1645	0.6851	9500.0	0.3415
Lyot (*n*=55)	2.1382	0.0659†	3.5507	0.0595†	25272.5	0.0265*
Scandia (*n*=257)	1.2371	0.4209	0.5160	0.4725	99649.0	0.2042
Utopia (*n*=229)	0.7279	0.3301	0.8589	0.3540	91472.5	0.1473

[a] *n* is the sample size of each geological province. Asterisks (*) indicate provinces where tests are significant at the 95% confidence level. Crosses (†) indicate provinces where tests are significant at the 90% confidence level.

regions at longitude 30°E and 270°E. The number of craters with detections of mafic and hydrated minerals is then compared to the total number of craters surveyed within that geological province (Figure 14b).

On average ~20–26% of craters show mafic detections and 5–10% show hydrated mineral detections in most of the geologic provinces. In Chryse Planitia, however, 71% of craters show mafic mineral detections, significantly higher than the rest of the northern lowlands. For hydrated detections, both Chryse Planitia and the vicinity of Lyot show a slightly higher percentage of hydrated mineral detections than the average northern lowlands. On the contrary, Arcadia Planitia has a paucity of mineral detections for both mafic and hydrated minerals. Mafic mineral detections within Chryse Planitia (+), Arcadia Planitia (−), and Utopia Planitia (−) are statistically different from the detections in the rest of the northern lowlands at the 95% confidence level from three statistical tests (Table 1) ("±" referring to more/less than average) (Figure 14). Hydrated mineral detections within Arcadia Planitia (−), Chryse Planitia (+), and Lyot vicinity (+) are statistically distinct at the 90% confidence level (Table 1). The differences in mineral occurrences associated with impact craters in these different regions are probably related to distinctive regional geologic histories since dichotomy formation and will be discussed in detail (see section 5.6).

4.3.3. Effect of Dust Cover on CRISM Detections

To better understand how the mineralogy detected by shortwave infrared data correlates with dust cover, we show the mineralogy detections plotted on a dust cover index map (DCI) derived from Thermal Emission Spectrometer (TES) data (Figure 15) [*Ruff and Christensen*, 2002] as well as the percentage of detections plotted against binned dust cover index (Figure 16). There is a strong negative correlation of mineral detections with the TES-determined dust cover, which confirms that our detections are concentrated in the more "dust-free" regions (Figure 15). Mineral detections are more prevalent where there is less dust cover relative to the sampled population of craters (Figure 16), except for the last few bins where sample size is small. This correlation implies obscuration of mineral signatures in high dust cover locations, which indicates the mafic and hydrated minerals associated with impact craters may be even more widespread than recognized from our analyses.

4.3.4. Crater Modification

Impact craters scattered throughout the northern lowlands have been modified due to erosion of crater rims and ejecta and infill of the crater floor, resulting in subdued crater forms with subtle rims, degraded or buried ejecta, and reduced depth to diameter ratios. Such processes mantle bedrock exposure and can prevent detection of the mineralogy of the impacted bedrock. Degradation state was assessed and recorded in a Mars crater database [*Robbins and Hynek*, 2012] as a quantized measure from class 1 to 4 ("1" being most degraded), depending on the sharpness and relief of crater rim, ejecta preservation, floor infilling, and relative depth/diameter ratio. We

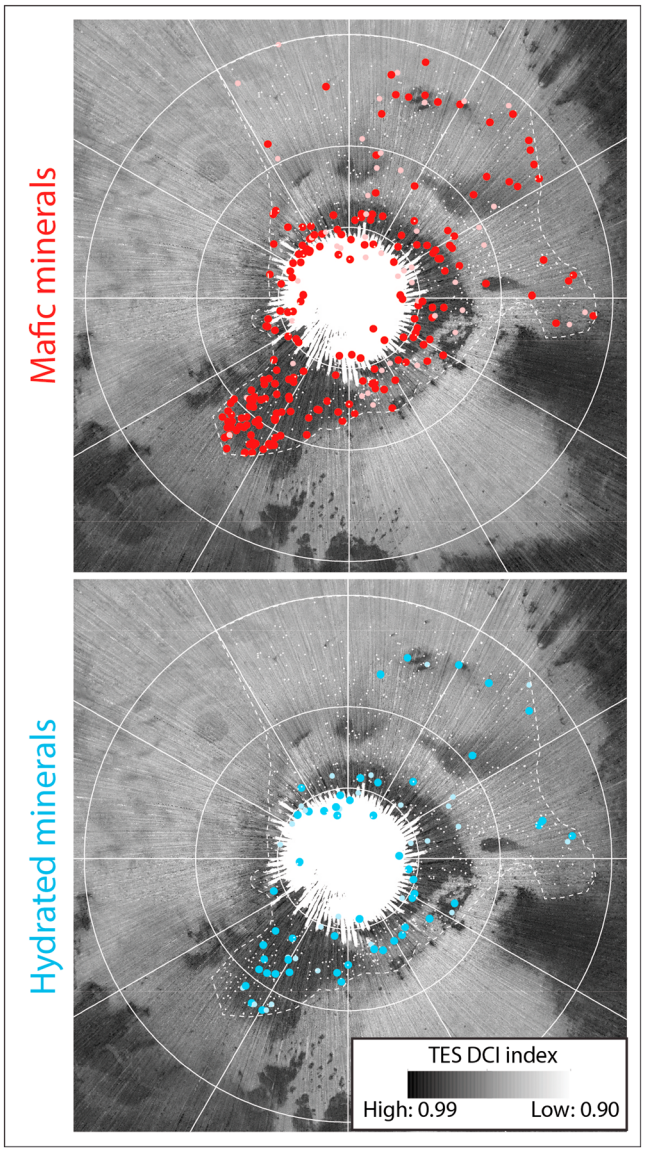

Figure 15. Mineral detections on a TES global dust index map with high dust cover in bright shades and low dust cover in dark shades. (Note that the formulation of dust cover index (DCI) is such that high DCI indicates less dusty and low DCI means dustier.) The base map is TES global dust cover index map of the northern hemisphere of Mars, in Mars North Polar Stereographic Projection.

find that the ratio of detections for both mafic and hydrated minerals increases with the preservation state; i.e., less degraded craters have a higher percentage of mineral detections (Figure 17).

4.3.5. Multivariate Statistical Significance of Different Factors

To understand the relative importance of the different factors that affect the mineral detections in the northern lowlands, we performed a multivariate statistical analysis on the mafic and hydrated detections as a function of crater size, dust index, and modification using a logistic function fit to evaluate the relative influence of each factor on the probability of detection. We evaluated the data for 487 (out of 1045) observations, filtered to remove craters with missing dust cover index or degradation state. We find that for both mafic and hydrated minerals, all of these factors are important to the identification of a mineral detection with a confidence level of 95%, which confirms that the final detection of a mafic or hydrated mineral is sensitive to dust cover and postimpact modification as well as crater diameter (Table 2).

5. Discussion

5.1. The Nature and Origin of Mafic Minerals

In the northern lowlands, mafic mineral detections are more prevalent than hydrated mineral detections (Figure 6), and olivine is more commonly detected than pyroxene (Figure 7). Olivine is more easily distinguished, possibly because the spectra are ratioed to the pyroxene-bearing surroundings. The greater prevalence of olivine detections in ratioed spectra is best interpreted as variability between olivine-rich and olivine-poor units. The commonly occurring olivine detections in the northern lowlands indicate that olivine-bearing volcanic rocks are widespread in the subsurface, confirming the previous identification of olivine-enriched deposits [*Salvatore et al.*, 2010; *Ody et al.*, 2013]. The lack of crystalline mafic minerals on the bulk surface of the northern lowlands indicates that the mafic mineral-bearing units were emplaced before the late Hesperian to Amazonian-aged surface plain materials [*Bibring et al.*, 2005; *Mustard et al.*, 2005].

The observed mafic mineralogy in the subsurface can be interpreted as unaltered transported outflow channel sediments filling the basin, which has been previously inferred from gravity data [e.g., *Zuber et al.*, 2000; *Phillips et al.*, 2001]. However, the spatial distribution of mafic minerals is not correlated with outflow channel sedimentation locations inferred from gravity data, but rather the mafic minerals are widespread across the entire northern lowlands. Overall, the buried mafic minerals revealed in the northern lowlands

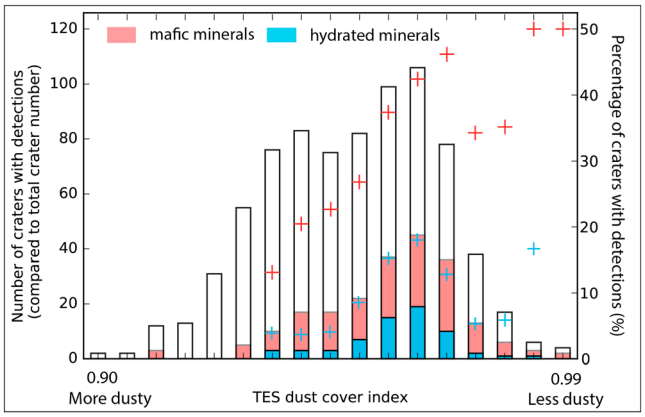

Figure 16. Correlation of mafic and hydrated mineral detections to the TES global dust index. The left axis is for the bar chart showing the number of craters with and without detections as a function of dust index. The right axis shows the percentage of mineral detections in all craters sampled, marked with the red and blue crosses for mafic and hydrated minerals.

impact craters and their distribution is more consistent with widespread volcanism in the northern hemisphere, as previously suggested [*Head and Kreslavsky*, 2002]. Our overall estimate of the volume of this volcanic unit is greater than that in prior works (see section 5.7).

5.2. The Nature and Origin of Hydrated Minerals

The survey of the impact craters of the northern lowlands revealed Fe/Mg smectite or mixed-layer clays, chlorite/prehnite, and hydrated silica as the most abundant identifiable hydrated phases in the northern lowlands, based on the number of occurrences (Figure 7), similar to the trends in the relative proportions of major hydrated minerals found in the southern highlands and other large-scale surveys [*Ehlmann et al.*, 2011, *Carter et al.*, 2013a; *Sun and Milliken*, 2015]. In our survey, Fe/Mg smectite is found in 32% of all the 81 craters with hydrated minerals, followed by silica (17%) and chlorite/prehnite (11%). These observations are similar in relative prevalence to a prior global survey of central peaks where they identified Fe/Mg smectite (in ~81.9% of all 444 hydrated central peak regions globally), followed by chlorite (26.8%) and hydrated silica (22.6%) [*Sun and Milliken*, 2015].

Interestingly, unidentified hydrated minerals are found in the majority of craters (~74%) with any hydrated mineral detection. This unidentified hydrated mineral class has been recognized previously but in much smaller proportion of their data set (found in only 6.8% of the southern highlands central peaks) [*Sun and Milliken*, 2015]. As discussed in *Sun and Milliken* [2015], the spectral signatures could be explained by zeolite, sulfate, or other hydrated salts. Poorly crystalline clays or quasi-amorphous materials with weaker metal-OH absorptions at 1.4 and 2.3 μm are other possibilities. H_2O can be added to or removed from many hydrated minerals, including the above, as a function of relative humidity. Thus, the particular spectral character in the north may be due to enhanced hydration (colder temperatures raising relative humidity, nearer ice table), resulting in a stronger 1.9 μm absorption with other weaker H_2O and metal-OH absorptions absent due to mixing, dust cover, or low signal to noise.

As with mafic minerals, the hydrated minerals found in large craters could be excavated from the subsurface. They could also form postimpact via hydrothermal systems, deposition in aqueous environments, or fluvial or aeolian transport from elsewhere. The strong correlation of hydrated minerals and large craters indicates that the formation or exposure mechanism for the majority of hydrated detections involves the energy of the impact directly. Among the 81 craters we identify here with possible hydrated/hydroxylated minerals, we find morphological evidence that indicates excavation processes related to the mineralogy, such as juxtaposed mafic and hydrated minerals in the central peaks and ejecta blankets (e.g. Figures 18a–18f of this work and Figures 3 and 4 of *Carter et al.* [2010]), uplifted bedrock collocated

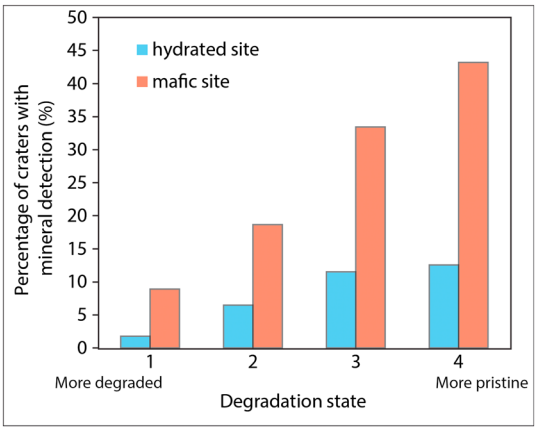

Figure 17. Percentage of craters with mineral detections as a function of the degradation state of craters.

Table 2. Regression Results From a Multivariate Binary Logistic Model of Different Factors in CRISM Survey[a]

Mineralogy	Mafic Mineral Detection		Hydrated Mineral Detection	
Factors	*z*-Stat	*p*-Value	*z*-Stat	*p*-Value
Diameter	3.40	0.0007*	5.33	0.0000*
Dust index	5.84	0.0000*	3.84	0.0001*
Degradation state	4.06	0.0000*	1.98	0.0481*
c	−6.19	0.0000	−4.18	0.0000

[a]Asterisks indicate influencing factors that are important to the number of detections with 95% confidence (*c* is a constant needed to fit the regression; it does not have a statistical significance).

with hydrated mineral detections (e.g., Figures 18c and 18e of this work, Figures 1d and 1e of *Gross et al*. [2015], and Figures 1 and 2 of *Pan and Ehlmann*, [2017]) or consistent mineralogy on the crater central peak, ejecta, and crater wall (e.g., Figure 18b). Though crater ejecta blankets are typically not preserved in the lowlands, we still observe ~15% of hydrated mineral detections in well-preserved crater ejecta (e.g., Figure 18f). Small craters ($D < 10$ km) that do not generate enough heat to produce a long-lived hydrothermal system expose hydrated mineral-bearing strata on crater walls, which represent subsurface material excavated by these craters. We also find the spatial distributions of mafic and hydrated mineral-bearing craters to be quite similar (Figures 6 and 15), largely controlled by dust cover and degradation, though hydrated minerals are found, on average, in larger craters. Together, the detections are consistent with excavation of the hydrated minerals from an ancient altered basement, as previously proposed [*Carter et al*., 2010].

It remains a possibility that some hydrated minerals may form during or postimpact for certain large, complex craters where geologic context of the mineral detections is less clear (as opposed to Figure 18 and examples in previous works), though at CRISM resolution, we were not able to resolve filled fractures in the central peak/ring region or morphology related to hydrothermal fluids during or post impact. Only in a few instances in previous works, large-scale sedimentary units allowed identification of postimpact hydrated mineral deposits [*Mangold et al*., 2012; *Sun and Milliken*, 2015], which have not been found in the northern lowlands in this study. With future orbital or in situ data acquired that resolve finer scale texture combined with mineralogy, we will be able to perform detailed mapping to establish the time relationship of the geological units in each crater and further distinguish the postimpact formation of hydrated/hydroxylated minerals. Recognizing and confirming the postimpact formation mechanisms for these minerals would have great implications for the Martian environment in the Amazonian. In the following discussion, we discuss the constraints on the stratigraphy of the northern lowlands based on the assumption of an excavation origin for the majority of the mafic and hydrated mineral occurrences.

5.3. Mineralogy of the Upper Layer of the Northern Lowlands

The surface units of the northern lowlands do not typically have the mafic absorption features of crystalline basaltic rock or the spectral features of hydrated/hydroxylated minerals. The upper layer encompasses a number of different geologic units: the Vastitas Borealis Formation covering Acidalia, Utopia, and Polar Scandia regions, Amazonian smoothed terrains in Amazonis, and Arcadia Planitia and Isidis basin filling materials. The units probably consist of a variety of materials including loess-like deposits [*Skinner et al*., 2012], sediments, lavas and/or volcaniclastic materials, yet the signals of hydrated or mafic mineralogy are not observed using CRISM data. Puzzling as it is, we suggest that the "bland" VSWIR spectral features of the upper layer may be due to either weathering products of basaltic glass with silica-enriched rinds [*Kraft et al*., 2003; *Horgan and Bell*, 2012] or alteration coatings of optically active Fe minerals in basalt, analogous to those observed at Gusev crater [*McSween et al*., 2006; *Mustard et al*., 2005; *Salvatore et al*., 2010]. Alternatively, these features may be due to poorly crystalline phases dominating the spectral properties, similar to the abundant amorphous material in unconsolidated sediments as well as sedimentary rocks within Gale crater as explored by the Curiosity rover [e.g., *Blake et al*., 2013; *Bish et al*., 2014].

5.4. Inferred Subsurface Stratigraphy Based on an Impact Excavation Model

Assuming an excavation origin of the observed mineralogy associated with impact craters, we apply impact crater models to provide insights into subsurface stratigraphy by exposing materials in the ejecta, walls, and central peaks.

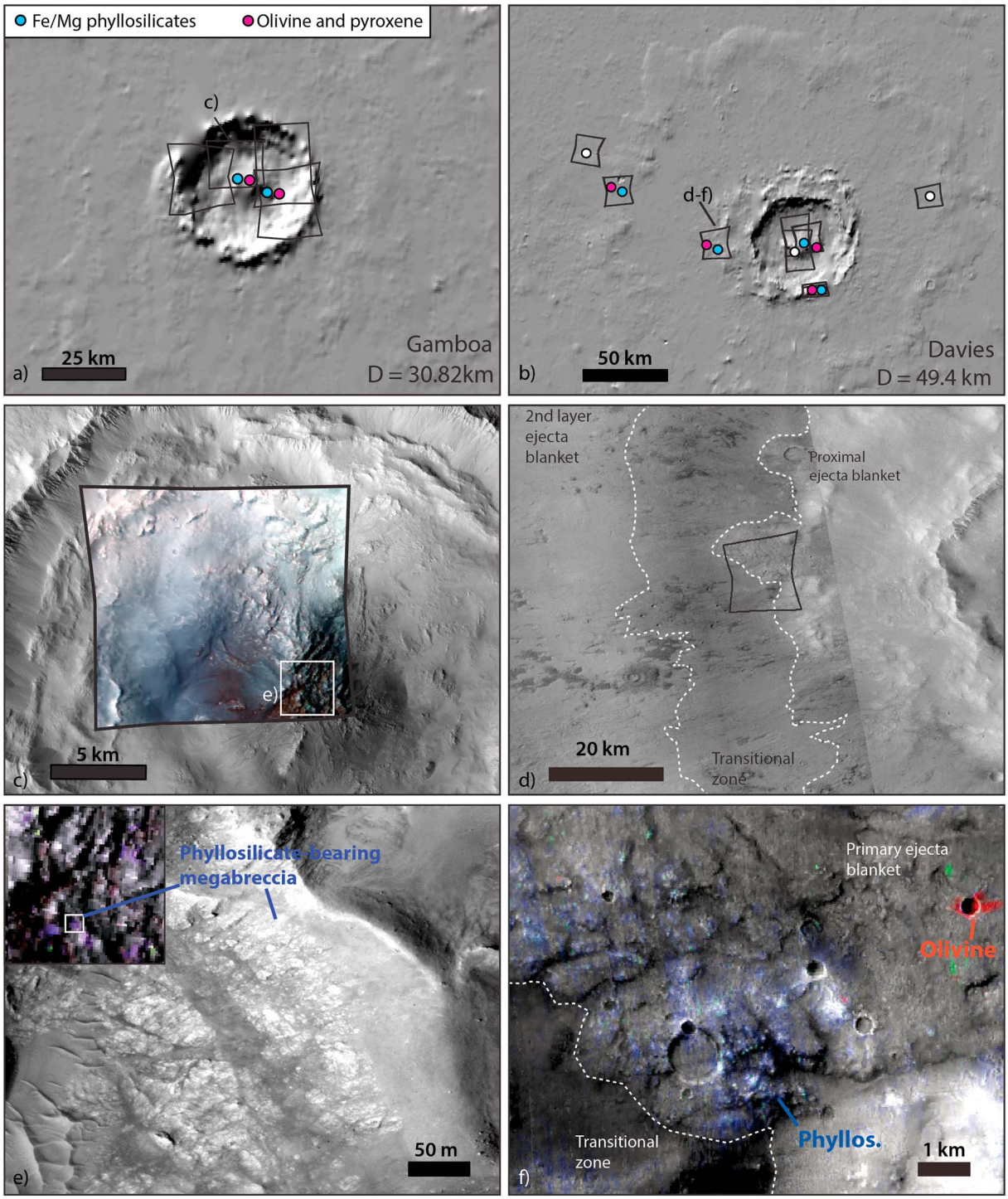

Figure 18. Examples of excavation of hydrated-mineral-bearing stratigraphy. (a) CRISM target footprints with mineral detections of Gamboa crater on a THEMIS nighttime infrared image mosaic as the base map; (b) CRISM target footprints with detections for Davies crater on a THEMIS nighttime infrared image mosaic as the base map. Notice that same mineralogy is found in crater central peak, crater walls, and ejecta blanket, consistent with an excavation origin. (c) CRISM false color image (HRS0000CA51) overlain on CTX mosaic of Gamboa crater. (d) The footprint of CRISM image (FRT00018AEF) on the transitional boundary of primary dissected ejecta blanket and the smooth and dark transitional units overlying the ejecta. (e) HiRISE image (ESP_028724_2210) showing the phyllosilicate-bearing uplifted bedrock units in the Gamboa crater central peak. In the upper left corner is the gray-scale CRISM image HRS0000CA51 zoom-in overlain by mineral parameter maps (R: Olivine, G: BD1900, B: BDMG), with the white outlined box showing the context for HiRISE image. (f) Zoom-in of CRISM image (FRT00018AEF) with color overlay (R: Olivine, G: BD1900, B: BDMG), showing the neighboring phyllosilicate and olivine detections on the ejecta blanket of Davies crater.

In the northern lowland survey, 14% of all mineral detections are found in crater ejecta, 41% in the central peak/ring region, 35% on crater wall/rim, and 10% in crater floor deposits. Scaling relationships from lab experiments and computational simulations can be applied to estimate the *maximum excavation depth* from the rim-to-rim diameter of the craters and place a lower bound of the starting position in the stratigraphy for the ejected materials. Some of the bedrock exposed in the central structure of a crater has an origin deeper than the *maximum depth of melting*, a calculable parameter [*Cintala and Grieve*, 1998]. A different empirical relationship predicts the original depth of uplifted material from observation of 24 terrestrial complex structures [*Grieve and Pilkington*, 1996; *Cintala and Grieve*, 1998] to be $0.086D^{1.03}$ (where D is the diameter of the crater) and has been applied to Mars [*Tornabene et al*., 2008; *Quantin et al*., 2012]. However, these parameters do not provide hard constraints on the original depth of materials observed in the final central peak, since near the center of the crater, elements of subsurface stratigraphy are mixed as observed in numerical models [*O'Keefe and Ahrens*, 1999]. The mineralogy exposed in the central peak/ring region represents a mixture of lithologies from the shallow subsurface to the unmelted deeper stratigraphy with the possibility also of sampling a deeper layer than the mineralogy seen in the ejecta and crater wall regions [e.g., *Ernst et al*., 2010].

Here we use the maximum excavation depth to place a constraint on the starting elevation of the materials in the central peak as well as ejecta, crater floor, and detections in the terraced rim of large complex crater, which could be mixed with proximal ejecta. The detections on the crater wall/rim of simple craters that originate from depths near the preimpact surface are treated differently, as described below. The maximum excavation depth ($d_{\text{max\_excavation}}$) is predicted by the static Maxwell Z model to be approximately 1/10 of the diameter of the transient crater ($D_{\text{transient}}$) (equation (3)) [*Melosh*, 1989].

$$d_{\text{max\_excavation}} = \frac{1}{10} D_{\text{transient}} \tag{3}$$

The diameter of the transient cavity is related to the final crater diameter (D_{final}) by a scaling relationship as shown in equation (4)

$$D_{\text{transient}} \cong a\,(D_{\text{final}})^{b} (D_{*})^{c} \tag{4}$$

D_{*} is the transition diameter from simple to complex crater on Mars, estimated to be ~8 km from observations [*Garvin and Frawley*, 1998], and a, b, and c are constants with three different parameterizations (Table 3) [*Melosh*, 1989; *Holsapple*, 1993; *Croft*, 1985]. For the diameter range of craters examined in this survey, the different parameterizations result in a difference of less than 500 m for estimated maximum excavation depth for more than 99% of all the craters. We use the parameterization based on *Holsapple* [1993], which gives the intermediate estimate for observed diameter range to calculate the maximum excavation depth for each crater. The excavation depth is then subtracted from the elevation of the preimpact surface, which is calculated as the median MOLA elevation of 4–5 locations at 2.5 crater radii outside the crater ejecta blanket (Figure 19). The only exception is the specific group of pedestal craters with elevation higher than the surrounding plains; for these, the elevation of crater floor is taken as a proxy for the elevation of the preimpact surface.

On the other hand, a small number of detections are found on the overturned flap on crater wall/rim of small, simple craters. These exposures represent deposits very close to the preimpact surface, and we use the elevation of the preexisting surface as a constraint on the upper bound of the original elevation of these deposits (Figure 19).

Assuming an excavation origin, the data show that the hydrated minerals may have originated from stratigraphic locations of −4 to −5.5 km or deeper relative to MOLA (Figure 19). In contrast, mafic mineral maximum excavation depths are found to range from ~100 m to several kilometers across the northern lowlands. In some locations, especially Chryse and Acidalia, mafic minerals exposed on the crater wall as part of the nondisrupted stratigraphy indicate very shallow (several meters) origin of these detections. The highest predicted stratigraphic location for hydrated mineral detections is consistently at lower elevation than that for mafic minerals (excluding the hydrated silica detections in small craters in Acidalia, which are not representative of the ancient basement, see section 5.6.2). The elevation difference between the highest occurrence of hydrated mineral detection and that of mafic detection in the same geological province gives a rough

Table 3. Scaling Parameters for the Diameter of the Transient Crater From Different Scaling Models

Parameters	*a*	*b*	*c*
Melosh, 1989	0.84 for simple crater 0.65 for complex	1	0
Holsapple, 1993	0.758	0.921	0.079
Croft, 1985	1	0.85	0.15

estimate of the thickness of mafic mineral-bearing layers—likely made up of several discrete mafic units. The estimated thickness is 1–2 km and varies across the plains, which is consistent with or deeper than the estimate from a prior lava filling model (0.8–1.0 km on average) [*Head and Kreslavsky*, 2002]. This layer with mafic minerals seems to be thicker in Utopia and Elysium Planitia than in Acidalia, Chryse, Lyot, or Scandia. Arcadia and Isidis have only a few mafic detections and no certain hydrated mineral detections, so the existence and depth of the mafic layer(s) and hydrated basement cannot be well constrained (Figure 19).

The thickness of the upper layer with no mineral detection may be highly variable across the entire lowland area. The layer is probably thinner (several meters to 100 m, consistent with previous estimates for VBF [*Kreslavsky and Head*, 2002; *Salvatore and Christensen*, 2014a]) in Acidalia and Chryse Planitia but much thicker (up to several km) in Lyot, Elysium, and Arcadia region, which may have had different resurfacing processes than the Vastitas Borealis Formation.

5.5. A Missing Mineralogy Record of a Global Northern Ocean?

On Earth, oceanic sediments include constituents originated from Earth's lithosphere, e.g., transported crustal materials, organic and inorganic biomaterials (some carbonates, some silica, and a small amount of organic matter), authigenic ferromanganesian minerals, and hydrated silicates (montmorillonite, illite, chlorite, zeolites, and smectites) [*Goldberg*, 1961]. If a long-lived ocean existed within the northern lowlands of Mars, it could form extensive hydrated silicate minerals like those on Earth through water-rock interaction. Also, as the ocean evaporated, dissolved chemical constituents could form salt deposits (including carbonate, sulfate, and chloride salts) similar to salt sediments on Earth where ancient lakes dried out [*Braitsch*, 1971].

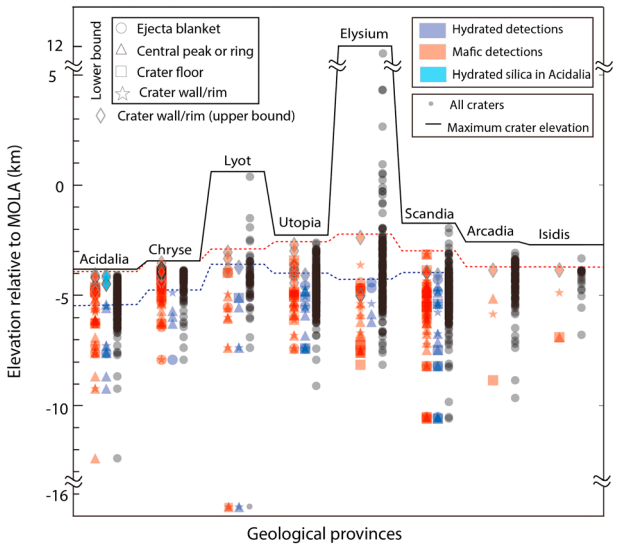

Figure 19. Origin depth of materials within different geological provinces in the northern lowlands assuming the excavation origin, as described in section 5.4. The solid black line indicates the elevation of the topographically highest crater in each geological province. The small black dots show the lower bound for the original elevation of excavated materials for each studied crater. Calculated lower bounds for mafic minerals (red), hydrated minerals (blue), and Acidalia hydrated silica (cyan) are plotted with different symbols for occurrences in crater ejecta (circle), crater central peak/ring (triangle), crater floor (square), and crater walls of complex craters (star). Some crater floor (square) detections may include deposits not directly related to excavated bedrock. Detections on the crater wall/rim of small, simple craters are plotted in diamonds and represent upper bounds on the elevation of origin. The colored dashed lines indicate the uppermost crater showing mafic (red) or hydrated (blue) minerals.

As summarized above, the stratigraphy we present in section 5.4 does not include a clear mineralogical record of a global northern ocean. There is no mineralogically distinct intermediate depth unit between the inferred basement and mafic units, nor between mafic units and surface units. We do not observe large-scale local concentrations of sulfates, hydrated salts, or carbonates, nor obvious clustering for Fe/Mg clays.

Carbonates, hydrated sulfates (gypsum and kieserite), and concentrated chloride deposits are readily detected by CRISM elsewhere on Mars [*Ehlmann and Edwards*, 2014] but are not found in craters in this survey of the northern lowlands. It is possible that some phyllosilicates in the lowlands could represent

detrital or authigenic minerals in the presence of an ocean, but no particular clustering in spatial distribution has been observed for the phyllosilicate detections (e.g., near outflow channels), and they have been found to co-occur with other higher temperature phases (e.g., prehnite), unrelated to the secondary alteration of an ocean. The lack of associated mineralogy does not completely preclude a northern ocean(s), but the data provide key constraints. If an ocean did exist, (a) the spatial and temporal extent of the "ocean" may have been limited, resulting in insufficient water-rock interaction for mineralization to be detectable from orbit (in contrast with southern highland lake deposits); (b) the water-rock interactions may have been kinetically inhibited due to lower temperature [e.g., *Fairén et al*., 2011]; (c) the liquid water may have had low ionic strength, resulting in limited salt formation as the ocean evaporated/froze; or a combination of these factors.

We considered whether the "hydrated unidentified" minerals might be a group of hydrated salts that represent remnants of a northern ocean. However, the distribution within the northern lowlands overlaps with other Fe/Mg phyllosilicate detections (Figure 10). No particular clusters have been identified in spatial distribution or original stratigraphic position as inferred from stratigraphic position, which does not suggest a different origin from the phyllosilicates. The few sulfate and zeolite detections made do suggest there are locations in the lowland region potentially with different forms of aqueous alteration from the hydrated basement. In any case, we did not discover widespread mineralogy in support of a long-lived global ocean, but if an ocean did exist in the northern lowlands, the formation of alteration minerals and salts could have been inhibited by the reasons above.

5.6. Regional Geological and Aqueous History Revealed by Impacts

Though mineralogical evidence of a northern ocean was not discovered, distinctive regional differences in mineralogy were revealed in a few select geologic provinces, described below.

5.6.1. Mafic Minerals in Chryse Planitia

Chryse Planitia and Acidalia Planitia are adjacent to one another and are both regions of interest because of the immense outflow channels that debouch into them and the water-related sedimentation features on the surface. Geological mapping has revealed widespread possible water-lain sediments on the surface of Chryse and Acidalia [*Tanaka*, 1997; *Salvatore and Christensen*, 2014b]. In this study, we find that beneath a thin layer of spectrally bland sediments, Chryse Planitia has a high occurrence rate of mafic detections compared to the rest of the northern lowlands. Specifically, the mineral detection rate differs substantially for small craters ($D < 10$ km) in Chryse and Acidalia, but much less for large craters (Figure 6).

There are at least three possible explanations for the mafic minerals in Chryse Planitia: a localized source of volcanic lava flows, mafic mineral-bearing outflow channel deposits, and better exposure due to less resurfacing and dust cover in the region. A relative depletion of mafic mineralogy in Acidalia compared to Chryse because of more deposition of the Vastitas Borealis Formation at higher latitudes seems consistent with larger depth/diameter ratio of craters in Chryse (~0.08) than Acidalia (~0.04). Yet the mafic detection rate in Acidalia is consistent with the rest of the northern lowlands, including areas like Elysium Planitia and Isidis Basin that have not been covered by the Vastitas Borealis Formation. Moreover, detections of hydrated minerals in several small craters in Acidalia confirm that exposures in smaller craters have not been completely obscured. Therefore, it is more likely the enhanced mafic detections represent a stratigraphic difference in Chryse Planitia rather than surface mantling effects. The mafic materials may result either from deposition of mafic mineral-bearing sediments from outflow channel deposits or from a source of volcanic materials that is not found in other parts of the lowlands. It is less likely that these are sedimentary deposits from outflow channels because alteration and sorting during transport tend to deplete or weather pristine olivine and produce less pronounced spectral features in the sediments relative to transported materials. If they are indeed sediments transported and deposited from outflow channel debouching, they represent a mafic mineral-enriched unit that has been transported in an environment where alteration is limited. Otherwise, these mafic units may represent deposits from volcanic activity directly. Since there is no obvious lava source in the vicinity of Chryse Planitia except for Tharsis, it is possible that a previously unrecognized source exists in/around Chryse (e.g., fissure eruptions). Interestingly, olivine has been identified in Ganges and Eos Chasma in the neighboring southern highlands in patchy deposits that can be traced as a layer [*Edwards et al*., 2008], which could potentially provide a source layer for the outflow channel deposits or be related to the same episode of effusive volcanic flow.

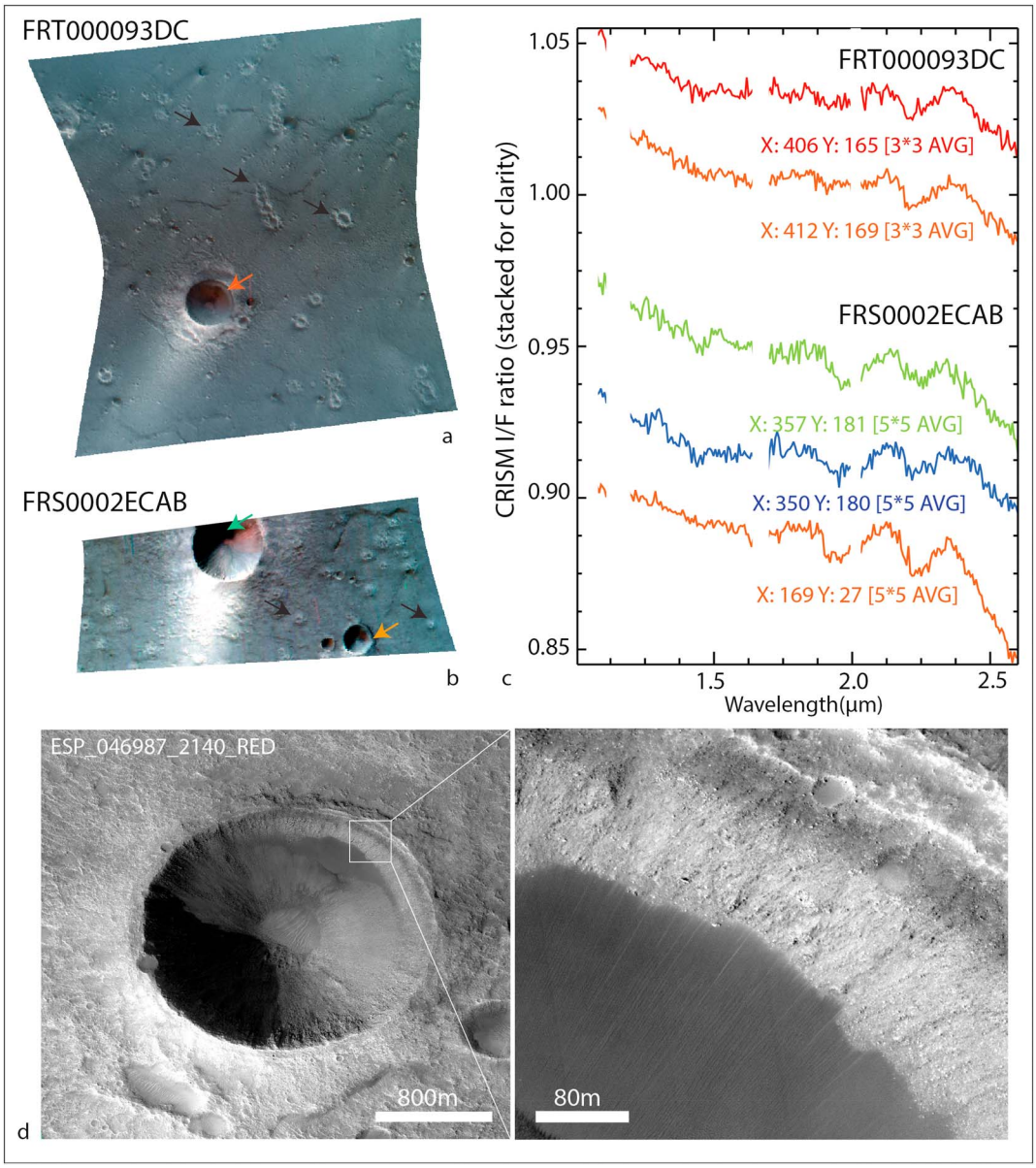

Figure 20. Hydrated silica detections in Acidalia Planitia, on Vastitas Borealis Formation boundary units with small degraded conical features (black arrows). (a) CRISM image FRT000093DC where hydrated silica is found as exposed on crater walls, consistent with the interpretation of an excavated shallow subsurface deposit. The arrows point to the locations where the spectra are taken from. (b) CRISM image FRS0002ECAB where silica is detected in two small craters (with diameters 1 km and 2.5 km). (c) Hydrated silica spectra from the CRISM images in Figures 20a and 20b. Absorption features are shaper, and 2.2 μm feature is wider for the smaller small crater (orange arrow) than larger one (green arrow) in FRS0002ECAB. (d) HiRISE coverage of crater in FRT000093DC with zoomed-in image showing the relatively high albedo and rocky texture of the silica-bearing layer with a layer extent of 80–100 m.

5.6.2. Silica Deposits in Small Craters in Acidalia

In Acidalia and Chryse Planitia, light-toned layers have been identified on walls of small craters that suggest widespread sedimentation in the shallow subsurface, possibly due to outflow channels [*Salvatore and Christensen*, 2014a]. In this study, we do not find evidence for any aqueous alteration related to these deposits, but there are four small craters (with diameters 1–2.5 km) at the boundary between Chryse and Acidalia, each of which shows hydrated silica detections (Figures 10 and 20). In CRISM image FRT000093DC, hydrated silica is exposed on the crater wall in a layer a few CRISM pixels thick (~10–100 m) close to the surface (Figures 20a and 20c). The silica-bearing layer appears to be shedding relatively high-albedo blocks from

the crater wall, as observed from HiRISE image (Figure 20d). The extent of the layer on the image spans for 80–100 m, with the lower boundary covered by dark sands. The size of the craters implies impact energy insufficient to generate a long-lived hydrothermal system, and the morphology of detections over crater rims is likely to be the result of excavation of a shallow, subsurface deposit.

Other than these four craters, most other hydrated mineral detections in Acidalia are phyllosilicates or unidentified hydrated minerals in craters with diameter larger than ~11 km. The small craters probably represent a distinct, shallow subsurface hydrated silica unit in southern Acidalia, likely postdating the formation of most phyllosilicates found in larger craters based on the relative position in the stratigraphy. Hydrated silica has also been identified on the surface in noncrater-related terrains [*Pan and Ehlmann*, 2014] within Acidalia Planitia, embaying and thus postdating phyllosilicate-bearing knobs, which is consistent to the inferred stratigraphy from impact crater detections in this survey. The silica deposits in the knobby terrains have been suggested to form via localized aqueous alteration due to vapor weathering, thin film leaching, or silicate weathering with surface or subsurface water, and similar processes could have resulted in the formation of the hydrated silica deposits in southern Acidalia Planitia. The spatial proximity of these hydrated detections to conical features in Vastitas Borealis Formation (Figure 20) indicates that they might have formed during the same episode of subsurface volatile mobility. It is also possible the shallow hydrated silica is related to outflow channel sedimentation since they are located at the termini of the large outflow channels.

5.6.3. Arcadia Province: Few Detections of Mafic or Hydrated Mineralogy

The Arcadia Province encompasses both Arcadia and Amazonis Planitiae, west of the Elysium province, and east of Acidalia Planitia. The topography of Amazonis Planitia is extremely flat with small surface slopes (1:10,000 over a distance of 800 km) [*Aharonson et al*., 1998], and wrinkle ridges that are widespread in other parts of the northern lowlands are obscured in this region [*Head and Kreslavsky*, 2002], possibly also due to multiple mantling units of Amazonian-aged smooth terrain as mapped by *Tanaka et al*. [2014]. In this region, mafic and hydrated mineral detections are both atypically scarce, which cannot solely be explained by a moderately enhanced dust cover. The craters are more degraded in Arcadia and Amazonis Planitiae, and the depth-to-diameter ratios of these craters are small (average ~ 0.05). These data support a late resurfacing event in Arcadia and Amazonis. Thus, the lack of mafic and hydrated mineral detections for craters of all sizes in Arcadia and Amazonis Planitiae observed in this survey agrees with a complex resurfacing history in this region, and the depth of the first occurring mafic mineral in craters indicates that this surface unit could have a thickness of 180–1340 m (Figure 19).

5.6.4. Scandia Region North of Arcadia

The Scandia region north of Arcadia, part of the Vastitas Borealis Formation in the geological map by *Tanaka et al*. [2005], hosts 66 craters with mafic detections and 23 with hydrated detections. Due to the high latitude of this region, many images are affected by ice or dark sand dunes from the Olympia Undae field, so they were usually excluded from previous surveys. However, we were able to find hydrated and mafic minerals in relatively "clean" images. Mafic minerals are found in craters with a wide range of diameters and indicate widespread volcanic materials. The hydrated minerals found in this region include Fe/Mg phyllosilicates, chlorite/prehnite, and mostly unidentified hydrated minerals. The hydrated mineral detections in the Scandia region discovered in this study are the highest latitude phyllosilicate detections on Mars.

The region sits in between the north polar plateau and the immense Alba Patera volcanic shield, largely covering the Vastitas Borealis plains with various Scandia landforms, including Scandia Colles (knobs or mesas), Cavis (irregular depressions), and Tholis (low rounded plateaus) [*Tanaka et al*., 2011]. After the emplacement of Vastitas Borealis Formation, a variety of resurfacing processes reshaped the surface of the Scandia region including emplacement of Alba Mons volcanic material. The knobs and mesas were first interpreted to be remnants of ancient materials projecting through younger units [*Tanaka and Scott*, 1987] but later suggested to be related to the warming of the volatile-rich sediments proximal to Alba Mons resulting in collapse, erosion, and mud volcanism [*Tanaka et al*., 2011], a process that could be related to the hydrated minerals found in small craters in this survey. It has been proposed that the gypsum at Olympia Undae may be sourced directly from this unit [*Tanaka et al*., 2008], though we do not detect gypsum in crater-exposed bedrock in the region.

5.7. Insights Into the Geologic and Aqueous History of the Northern Lowlands

The impact crater mineralogy detected in the northern lowlands provides new insights into its geologic and aqueous history. The widespread hydrated minerals found in the largest craters are evidence for hydrated

components in the deep subsurface of the northern lowlands, indicating aqueous alteration of an ancient basement (likely Noachian or pre-Noachian). The basement is continuous and widespread in the northern lowlands at an elevation of −4 to −5.5 km, consistent with early formation of the crustal dichotomy, the topographic low, and subsequent burial by the plain materials. The most frequently found hydrated minerals are Fe/Mg phyllosilicate (smectite), chlorite/prehnite, hydrated silica, and numerous unidentified hydrated minerals, similar to the southern highlands with the lack of pervasive carbonate or salt deposits. Together this indicates that a northern ocean is not necessary to account for the hydrated mineralogy seen in the northern lowlands. If a northern ocean did exist, the water ionic strength may be low and the duration or temperature may have limited mineralization of ocean sediments.

Meanwhile, clay minerals, especially Fe/Mg smectite, are expected to undergo transformation into more stable mineral forms like chlorite under burial over several hundred million years on Earth [e.g., *Boles and Franks*, 1979; *Weaver*, 1989]. The temperature at a depth of 2 km could vary from 35 to 90°C for estimated geothermal gradients in the Noachian, depending on surface temperature [*Borlina et al*., 2015], encompassing the typical transition temperatures from Fe/Mg smectite to illite or chlorite on Earth [e.g., *Velde*, 1985]. The preservation of the juvenile mineralogy in the northern lowlands, similar to the southern highlands, indicates a weak geothermal gradient and/or low surface temperature since time of burial or the lack of postdepositional water for diagenetic maturation or both [*Tosca and Knoll*, 2009].

Mafic mineral detections in 251 impact craters are consistent with the previous suggestion of extensive volcanic materials in the northern lowlands subsurface. The extent of the mafic detections in craters covers an estimated surface area of ~66.7×10^6 km^2, more than doubling the area covered by Hesperian lava plains in the lowlands indicated by wrinkle ridges (~24.2×10^6 km^2) [*Head and Kreslavsky*, 2002]. In particular, the widespread olivine detections indicate that the Hesperian widespread lava plains in the lowlands may be related to the Early Hesperian aged olivine-bearing lava flows found in the southern highlands [*Ody et al*., 2013]. Using the inferred thickness of the mafic-bearing layer for each geological province, the extent of the mafic-bearing layer yields an estimate of ~$1–4 \times 10^7$ km^3 for the volume of volcanic materials in the subsurface of the northern lowlands, as much as the previous estimates of Hesperian lava flows globally (~3.3×10^7 km^3, including highlands [*Head and Kreslavsky*, 2002]). Volatile release from volcanic activity has been suggested to be capable of increasing the atmospheric pressure to ~0.3 bar and may induce transient warming effects [*Greeley*, 1987; *Craddock and Greeley*, 2009; *Halevy and Head*, 2014]. Although the overall effect on climate is debated due to the complication of competing cooling effects from aerosols [e.g., *Kerber et al*., 2015], the voluminous deposits in the northern lowlands indicate increased volatile release throughout the history of Mars and may have played important role in the early climate on Mars.

During the late Hesperian and through the Amazonian ages, many regional resurfacing events, not plain-wide filling, were dominant in shaping the northern lowland surface. Specifically, we have found that localized aqueous alteration in Acidalia formed hydrated silica deposits. Regional volcanic and/or sedimentary activity subsequently resurfaced Chryse Planitia, forming the mafic minerals. These hydrated silica and mafic minerals predate the sedimentation of a thin layer with no specific mineral detection, previously recognized as the Vastitas Borealis Formation. Arcadia and Amazonis Planitiae, however, were probably heavily resurfaced in middle-to-late Amazonian by loess, aeolian sediments, lavas, or pyroclastic deposits, forming the smooth terrains unit that filled in the majority of craters in the region. It is yet unclear how these events relate to the surface morphologic features observed (cones, polygons, and VBF), but the active geologic processes observed in the northern lowlands drive future studies to better understand Mars in the late Hesperian and Amazonian.

6. Conclusions

Here we summarize the main conclusions from the survey of impact crater mineralogy in the northern lowlands of Mars:

1. We observe mafic and hydrated minerals associated with impact craters in all of the major provinces in the northern lowlands.
2. Hydrated and mafic mineral detections are both positively correlated with crater size. Mafic minerals are more widespread in smaller craters (>~1 km), while hydrated minerals are mostly detected in the larger craters (>~29 km) with a much lower probability of occurrence in small craters. The relationship of crater

size to hydrated minerals suggests that they may represent an underlying hydrated basement excavated by large impact craters. We have not positively identified the formation of hydrated minerals via impact-induced hydrothermal alteration, but it remains a possibility to explain some of the data.

3. We have identified hydrated minerals in 81 out of 1045 craters examined in the northern lowlands, including Fe/Mg phyllosilicates, chlorite/prehnite, and hydrated silica. The presence of hydrated minerals in the Scandia region north of Arcadia is a new discovery. The frequency statistics of hydrated mineral phases are similar to those determined for southern highlands observations and global statistics except for the significantly greater prevalence of unidentified hydrated phases, where the exact mineral phase responsible for a 1.9 μm H_2O absorption cannot be identified.
4. Mafic mineral detections are widespread in all northern lowlands basins and are consistent with a substantial depth and volume of volcanic materials. The observed thickness of mafic-hosting materials implies volumes of volcanic materials in the northern lowlands ($1–4 \times 10^7$ km^3) could reach more than previous global estimates including highlands ($\sim 3.3 \times 10^7$ km^3).
5. No strong evidence for pervasive carbonate or other evaporative salts has been found to support the hypothesis of a global ocean. Instead, the hydrated minerals (in particular Fe/Mg phyllosilicates) detected are probably mostly related to an ancient Noachian basement, excavated from a depth of −4 to −5.5 km relative to the MOLA datum and similar in composition to the southern highlands.
6. Different regions of the northern lowlands show differences in the frequency of occurrences of mineral detections. Chryse Planitia has a significantly higher number of detections of mafic minerals, especially in small craters, which could be related to Tharsis volcanic products or other unrecognized volcanic sources. Small craters with hydrated silica detections are found in central Acidalia Planitia, representing younger and localized aqueous mineral formation. Amazonis and Arcadia Planitiae lack both mafic and hydrated detections, possibly due to later burial by the resurfacing events.
7. Further investigation of individual craters or regions will provide important insights into the local stratigraphy or aqueous activity specific to each crater or region in addition to the aqueous and geologic history of the northern lowlands.

Acknowledgments
The data supporting the analysis and conclusions have been included in the supporting information, and the processing details will be provided upon request. This work has been fully supported by NASA Mars Data Analysis Program grant NNX12AJ43G. We would also like to thank the CRISM team for targeting and providing the data set, as well as internal reviews that helped shape the early stages of the manuscript. The author also appreciates help from Kelsey Logan in data processing and insights on the statistics of data from Shasha Tong and Qiong Zhang. This manuscript was improved by thoughtful and constructive reviews from Nicolas Mangold and an anonymous reviewer.

References

Abramov, O., and D. A. Kring (2005), Impact-induced hydrothermal activity on early Mars, *J. Geophys. Res.*, *110*, E12S09, doi:10.1029/2005JE002453.

Aharonson, O., M. T. Zuber, G. A. Neumann, and J. W. Head (1998), Mars: Northern hemisphere slopes and slope distributions, *Geophys. Res. Lett.*, *25*, 4413–4416, doi:10.1029/1998GL900057.

Anderson, J. H., and K. A. Wickersheim (1964), Near infrared characterization of water and hydroxyl groups on silica surfaces, *Surf. Sci.*, *2*, 252–260, doi:10.1016/0039-6028(64)90064-0.

Andrews-Hanna, J. C., M. T. Zuber, and W. B. Banerdt (2008), The Borealis basin and the origin of the Martian crustal dichotomy, *Nature*, *453*(7199), 1212–1215, doi:10.1038/nature07011.

Baker, V. R., R. G. Strom, V. C. Gulick, J. S. Kargel, G. Komatsu, and V. S. Kale (1991), Ancient oceans, ice sheets and the hydrological cycle on Mars, *Nature*, *352*(6336), 589–594, doi:10.1038/352589a0.

Bandfield, J. L., V. E. Hamilton, and P. R. Christensen (2000), A global view of Martian surface compositions from MGS-TES, *Science*, *287*(5458), 1626–1630, doi:10.1126/science.287.5458.1626.

Baratoux, D., P. Pinet, A. Gendrin, L. Kanner, J. Mustard, Y. Daydou, J. Vaucher, and J.-P. Bibring (2007), Mineralogical structure of the subsurface of Syrtis Major from OMEGA observations of lobate ejecta blankets, *J. Geophys. Res.*, *112*, E08S05, doi:10.1029/2007JE002890.

Barnhart, C. J., and F. Nimmo (2011), Role of impact excavation in distributing clays over Noachian surfaces, *J. Geophys. Res.*, *116*, E01009, doi:10.1029/2010JE003629.

Bibring, J. P., et al. (2005), Mars surface diversity as revealed by the OMEGA/Mars Express observations, *Science*, *307*(5715), 1576–1581, doi:10.1126/science.1108806.

Bish, D., D. Blake, D. Vaniman, P. Sarrazin, T. Bristow, C. Achilles, P. Dera, S. Chipera, J. Crisp, and R. T. Downs (2014), The first X-ray diffraction measurements on Mars, *IUCrJ*, *1*(6), 514–522.

Bishop, J., J. Madejova, P. Komadel, and H. Froschl (2002), The influence of structural Fe, Al and Mg on the infrared OH bands in spectra of dioctahedral smectites, *Clay Miner.*, *37*(4), 607–616, doi:10.1180/0009855023740063.

Bishop, J. L., M. D. Lane, M. D. Dyar, and A. J. Brown (2008), Reflectance and emission spectroscopy study of four groups of phyllosilicates: Smectites, kaolinite-serpentines, chlorites and micas, *Clay Miner.*, *43*(1), 35–54, doi:10.1180/claymin.2008.043.1.03.

Blake, D. F., et al. (2013), Curiosity at Gale Crater, Mars: Characterization and analysis of the Rocknest sand shadow, *Science*, *341*(6153), doi:10.1126/science.1239505.

Boles, J. R., and S. G. Franks (1979), Clay diagenesis in Wilcox sandstones of southwest Texas: Implications of smectite diagenesis on sandstone cementation, *J. Sediment. Petrol.*, *49*(1), 55–70.

Borlina, C. S., B. L. Ehlmann, and E. S. Kite (2015), Modeling the thermal and physical evolution of Mount Sharp's sedimentary rocks, Gale Crater, Mars: Implications for diagenetic minerals on the MSL Curiosity Rover traverse, *J. Geophys. Res. Planets*, *120*, 1396–1414, doi:10.1002/2015JE004799.

Boynton, W. V., et al. (2007), Concentration of H, Si, Cl, K, Fe, and Th in the low- and mid-latitude regions of Mars, *J. Geophys. Res.*, *112*, E12S99, doi:10.1029/2007JE002887.

Braitsch, O. (1971), Salt deposits their origin and composition, vol. 4, Springer, Berlin, doi:10.1007/978-3-642-65083-3.
Budney, C. J., and P. G. Lucey (1998), Basalt thickness in Mare Humorum: The crater excavation method, *J. Geophys. Res.*, *103*, 16,855–16,870, doi:10.1029/98JE01602.
Burns, R. G. (1970), Crystal field spectra and evidence of cation ordering in olivine minerals, *Am. Mineral.*, *55*(9–10), 1608.
Carr, M. H., and J. W. Head (2003), Oceans on Mars: An assessment of the observational evidence and possible fate, *J. Geophys. Res.*, *108*(E5), 5042, doi:10.1029/2002JE001963.
Carter, J., F. Poulet, J. P. Bibring, and S. Murchie (2010), Detection of hydrated silicates in crustal outcrops in the Northern Plains of Mars, *Science*, *328*(5986), 1682–1686, doi:10.1126/science.1189013.
Carter, J., F. Poulet, J. P. Bibring, N. Mangold, and S. Murchie (2013a), Hydrous minerals on Mars as seen by the CRISM and OMEGA imaging spectrometers: Updated global view, *J. Geophys. Res. Planets*, *118*, 831–858, doi:10.1029/2012JE004145.
Carter, J., F. Poulet, S. Murchie, and J. P. Bibring (2013b), Automated processing of planetary hyperspectral datasets for the extraction of weak mineral signatures and applications to CRISM observations of hydrated silicates on Mars, *Planet Space Sci.*, *76*, 53–67, doi:10.1016/j.pss.2012.11.007.
Caudill, C. M., L. L. Tornabene, A. S. McEwen, S. Byrne, L. Ojha, and S. Mattson (2012), Layered MegaBlocks in the central uplifts of impact craters, *Icarus*, *221*(2), 710–720, doi:10.1016/j.icarus.2012.08.033.
Christensen, P. R., et al. (2001), Mars Global Surveyor Thermal Emission Spectrometer Experiment: Investigation description and surface science results, *J. Geophys. Res.*, *106*, 23,823–23,871, doi:10.1029/2000JE001370.
Cintala, M. J., and R. A. F. Grieve (1998), Scaling impact melting and crater dimensions: Implications for the lunar cratering record (vol 33, pg 889, 1998), *Meteorit. Planet Sci.*, *33*(6), 1343–1343.
Clark, R. N. (1999), Spectroscopy of rocks and minerals, and principles of spectroscopy, *Manual of Remote Sensing*, *3*, 3–58.
Clark, R. N., and T. L. Roush (1984), Reflectance spectroscopy-quantitative-analysis techniques for remote-sensing applications, *J. Geophys. Res.*, *89*, 6329–6340, doi:10.1029/JB089iB07p06329.
Clark, R. N., G. A. Swayze, R. Wise, K. E. Livo, T. Hoefen, R. F. Kokaly, and S. J. Sutley (2007), USGS digital spectral library splib06a, U.S. Geol. Surv., Digital Data Ser., 231.
Clifford, S. M., and T. J. Parker (2001), The evolution of the Martian hydrosphere: Implications for the fate of a primordial ocean and the current state of the northern plains, *Icarus*, *154*(1), 40–79, doi:10.1006/icar.2001.6671.
Craddock, R. A., and R. Greeley (2009), Minimum estimates of the amount and timing of gases released into the Martian atmosphere from volcanic eruptions, *Icarus*, *204*(2), 512–526, doi:10.1016/j.icarus.2009.07.026.
Croft, S. K. (1985), The scaling of complex craters, *J. Geophys. Res.*, *90*, C828–C842, doi:10.1029/JB090iS02p0C828.
Di Achille, G., and B. M. Hynek (2010), Ancient ocean on Mars supported by global distribution of deltas and valleys, *Nat. Geosci.*, *3*(7), 459–463, doi:10.1038/ngeo891.
Ehlmann, B. L., and C. S. Edwards (2014), Mineralogy of the Martian Surface, *Annu. Rev. Earth Planet. Sci*, *42*, 291–315, doi:10.1146/annurev-earth-060313-055024.
Ehlmann, B. L., et al. (2009), Identification of hydrated silicate minerals on Mars using MRO-CRISM: Geologic context near Nili Fossae and implications for aqueous alteration, *J. Geophys. Res.*, *114*, E00D08, doi:10.1029/2009JE003339.
Ehlmann, B. L., J. F. Mustard, S. L. Murchie, J. P. Bibring, A. Meunier, A. A. Fraeman, and Y. Langevin (2011), Subsurface water and clay mineral formation during the early history of Mars, *Nature*, *479*(7371), 53–60, doi:10.1038/Nature10582.
Ernst, C. M., S. L. Murchie, O. S. Barnouin, M. S. Robinson, B. W. Denevi, D. T. Blewett, J. W. Head, N. R. Izenberg, S. C. Solomon, and J. H. Roberts (2010), Exposure of spectrally distinct material by impact craters on Mercury: Implications for global stratigraphy, *Icarus*, *209*(1), 210–223, doi:10.1016/j.icarus.2010.05.022.
Fairén, A. G., A. F. Davila, L. Gago-Duport, J. D. Haqq-Misra, C. Gil, C. P. McKay, and J. F. Kasting (2011), Cold glacial oceans would have inhibited phyllosilicate sedimentation on early Mars, *Nat. Geosci.*, *4*(10), 667–670, doi:10.1038/ngeo1243.
Farrand, W. H., L. R. Gaddis, and L. Keszthelyi (2005), Pitted cones and domes on Mars: Observations in Acidalia Planitia and Cydonia Mensae using MOC, THEMIS, and TES data, *J. Geophys. Res.*, *110*, E05005, doi:10.1029/2004JE002297.
Frey, H. (2008), Ages of very large impact basins on Mars: Implications for the late heavy bombardment in the inner solar system, *Geophys. Res. Lett.*, *35*, L13203, doi:10.1029/2008GL033515.
Frey, H., B. L. Lowry, and S. A. Chase (1979), Pseudocraters on Mars, *J. Geophys. Res.*, *84*(B14), 8075–8086, doi:10.1029/JB084iB14p08075.
Frey, H. V. (2006), Impact constraints on the age and origin of the lowlands of Mars, *Geophys. Res. Lett.*, *33*(8), 2004–2007, doi:10.1029/2005GL024484.
Frey, H. V., J. H. Roark, K. M. Shockey, E. L. Frey, and S. E. H. Sakimoto (2002), Ancient lowlands on Mars, *Geophys. Res. Lett.*, *29*(10), 1384, doi:10.1029/2001GL013832.
Fuller, E. R., and J. W. Head (2002), Amazonis Planitia: The role of geologically recent volcanism and sedimentation in the formation of the smoothest plains on Mars, *J. Geophy. Res.*, *107*(E10), 5081, doi:10.1029/2002JE001842.
Garvin, J. B., and J. J. Frawley (1998), Geometric properties of Martian impact craters: Preliminary results from the Mars Orbiter Laser Altimeter, *Geophys. Res. Lett.*, *25*, 4405–4408, doi:10.1029/1998GL900177.
Goldberg, E. D. (1961), Chemical and mineralogical aspects of deep-sea sediments, *Phys. Chem. Earth.*, *4*, 281–302.
Greeley, R. (1987), Release of juvenile water on Mars—Estimated amounts and timing associated with volcanism, *Science*, *236*(4809), 1653–1654, doi:10.1126/science.236.4809.1653.
Grieve, R. a F., and M. Pilkington (1996), The signature of terrestrial impacts, *AGSO J. Aust. Geol. Geophys.*, *16*(4), 399–420, doi:10.2307/270718.
Gross, C., J. Carter, L. L. Tornabeme, M. Sowe and J. L. Bishop (2015), Stratified phyllosilicate-bearing deposits within impact craters in the Northern Plains of Mars. Lunar and Planet. Sci. Conf.
Halevy, I., and J. W. Head III (2014), Episodic warming of early Mars by punctuated volcanism, *Nat. Geosci.*, *7*(12), 865–868, doi:10.1038/ngeo2293.
Hartmann, W. K., and D. C. Berman (2000), Elysium Planitia lava flows: Crater count chronology and geological implications, *J. Geophys. Res.*, *105*, 15,011–15,025, doi:10.1029/1999JE001189.
Hazen, R. M., P. M. Bell, and H. K. Mao (1978), Effects of compositional variation on absorption spectra of lunar pyroxenes, Lunar and Planet. Sci. Conf.
Head, J. W., and M. A. Kreslavsky (2002), Northern lowlands of Mars: Evidence for widespread volcanic flooding and tectonic deformation in the Hesperian period, *J. Geophys. Res.*, *107*(E1), 5003, doi:10.1029/2000JE001445.
Hiesinger, H., and J. W. Head (2000), Characteristics and origin of polygonal terrain in southern Utopia Planitia, Mars: Results from Mars Orbiter Laser Altimeter and Mars Orbiter Camera data, *J. Geophys. Res.*, *105*, 11,999–12,022, doi:10.1029/1999JE001193.
Holsapple, K. (1993), The scaling of impact processes in planetary sciences, *Annu. Rev. Earth Planet. Sci.*, *21*, 333–373.

Horgan, B., and J. F. Bell III (2012), Widespread weathered glass on the surface of Mars, *Geology*, *40*(5), 391–394, doi:10.1130/g32755.1.
Karunatillake, S., et al. (2006), Composition of northern low-albedo regions of Mars: Insights from the Mars Odyssey Gamma Ray Spectrometer, *J. Geophys. Res.*, *111*, E03S05, doi:10.1029/2006JE002675.
Kerber, L., F. Forget, and R. Wordsworth (2015), Sulfur in the early martian atmosphere revisited: Experiments with a 3-D Global Climate Model, *Icarus*, *261*, 133–148, doi:10.1016/j.icarus.2015.08.011.
Klima, R. L., C. M. Pieters, and M. D. Dyar (2007), Spectroscopy of synthetic Mg-Fe pyroxenes I: Spin-allowed and spin-forbidden crystal field bands in the visible and near-infrared, *Meteorit. Planet. Sci.*, *42*(2), 235–253, doi:10.1111/j.1945-5100.2007.tb00230.x.
Klima, R. L., M. D. Dyar, and C. M. Pieters (2011), Near-infrared spectra of clinopyroxenes: Effects of calcium content and crystal structure, *Meteorit. Planet. Sci.*, *46*(3), 379–395, doi:10.1111/j.1945-5100.2010.01158.x.
Kraft, M. D., J. R. Michalski, and T. G. Sharp (2003), Effects of pure silica coatings on thermal emission spectra of basaltic rocks: Considerations for Martian surface mineralogy, *Geophys. Res. Lett.*, *30*(24), 2288, doi:10.1029/2003GL018848.
Kreslavsky, M. A., and J. W. Head (2002), Fate of outflow channel effluents in the northern lowlands of Mars: The Vastitas Borealis Formation as a sublimation residue from frozen ponded bodies of water, *J. Geophys. Res.*, *107*(E12), 5121, doi:10.1029/2001JE001831.
Lucchitta, B. K., H. M. Ferguson, and C. Summers (1986), Sedimentary deposits in the Northern Lowland Plains, Mars, *J. Geophys. Res.*, *91*, E166–E174, doi:10.1029/JB091iB13p0E166.
Malin, M. C., and K. S. Edgett (1999), Oceans or seas in the Martian northern lowlands: High resolution imaging tests of proposed coastlines, *Geophys. Res. Lett.*, *26*, 3049–3052, doi:10.1029/1999GL002342.
Mangold, N., S. Maurice, W. C. Feldman, F. Costard, and F. Forget (2004), Spatial relationships between patterned ground and ground ice detected by the neutron spectrometer on Mars, *J. Geophys. Res.*, *109*, E08001, doi:10.1029/2004JE002235.
Mangold, N., J. Carter, F. Poulet, E. Dehouck, V. Ansan, and D. Loizeau (2012), Late Hesperian aqueous alteration at Majuro crater, Mars, *Planet. Space Sci.*, *72*(1), 18–30, doi:10.1016/j.pss.2012.03.014.
Marinova, M. M., O. Aharonson, and E. Asphaug (2008), Mega-impact formation of the Mars hemispheric dichotomy, *Nature*, *453*(7199), 1216–1219, doi:10.1038/nature07070.
McGill, G. E., and L. S. Hills (1992), Origin of giant Martian polygons, *J. Geophys. Res.*, *97*, 2633–2647, doi:10.1029/91JE02863.
McSween, H. Y., et al. (2006), Characterization and petrologic interpretation of olivine-rich basalts at Gusev Crater, Mars, *J. Geophys. Res.*, *111*, E02S10, doi:10.1029/2005JE002477.
Melosh, H. J. (1989), *Impact Cratering: A Geologic Process*, Research supported by NASA, *Oxford Monogr. Geol. Geophys.*, vol. 11, 253 pp., Oxford Univ. Press, New York.
Michalski, J. R., M. D. Kraft, T. G. Sharp, L. B. Williams, and P. R. Christensen (2005), Mineralogical constraints on the high-silica Martian surface component observed by TES, *Icarus*, *174*(1), 161–177, doi:10.1016/j.icarus.2004.10.022.
Milliken, R. E., et al. (2008), Opaline silica in young deposits on Mars, *Geology*, *36*(11), 847–850.
Murchie, S. L., et al. (2009), Compact Reconnaissance Imaging Spectrometer for Mars investigation and data set from the Mars Reconnaissance Orbiter's primary science phase, *J. Geophys. Res.*, *114*, E00D07, doi:10.1029/2009JE003344.
Mustard, J. F., F. Poulet, A. Gendrin, J. P. Bibring, Y. Langevin, B. Gondet, N. Mangold, G. Bellucci, and F. Altieri (2005), Olivine and pyroxene diversity in the crust of Mars, *Science*, *307*(5715), 1594–1597, doi:10.1126/science.1109098.
O'Keefe, J. D., and T. J. Ahrens (1999), Complex craters: Relationship of stratigraphy and rings to impact conditions, *J. Geophys. Res.*, *104*, 27,091–27,104, doi:10.1029/1998JE000596.
Ody, A., F. Poulet, J.-P. Bibring, D. Loizeau, J. Carter, B. Gondet, and Y. Langevin (2013), Global investigation of olivine on Mars: Insights into crust and mantle compositions, *J. Geophys. Res. Planets*, *118*, 234–262, doi:10.1029/2012JE004149.
Oehler, D. Z., and C. C. Allen (2010), Evidence for pervasive mud volcanism in Acidalia Planitia, Mars, *Icarus*, *208*(2), 636–657, doi:10.1016/J.Icarus.2010.03.031.
Oehler, D. Z., and C. C. Allen (2012), Giant polygons and mounds in the lowlands of Mars: Signatures of an ancient ocean?, *Astrobiology*, *12*(6), 601–615, doi:10.1089/ast.2011.0803.
Pan, L., and B. L. Ehlmann (2014), Phyllosilicate and hydrated silica detections in the knobby terrains of Acidalia Planitia, northern plains, Mars, *Geophys. Res. Lett.*, *41*, 1890–1898, doi:10.1002/2014GL059423.
Pan, L., and B. L. Ehlmann (2017), Aqueous alteration from diverse hydrated minerals in Lyot crater and its vicinity, Lunar and Planet. Sci. Conf.
Parker, T. J., D. S. Gorsline, R. S. Saunders, D. C. Pieri, and D. M. Schneeberger (1993), Coastal geomorphology of the Martian Northern Plains, *J. Geophys. Res.*, *98*, 11,061–11,078, doi:10.1029/93JE00618.
Parker, T. J., R. S. Saunders, and D. M. Schneeberger (1989), Transitional morphology in west Deuteronilus Mensae, Mars—Implications for modification of the lowland upland boundary, *Icarus*, *82*(1), 111–145, doi:10.1016/0019-1035(89)90027-4.
Pelkey, S. M., et al. (2007), CRISM multispectral summary products: Parameterizing mineral diversity on Mars from reflectance, *J. Geophys. Res.*, *112*, E08S14, doi:10.1029/2006JE002831.
Perron, J. T., J. X. Mitrovica, M. Manga, I. Matsuyama, and M. A. Richards (2007), Evidence for an ancient Martian ocean in the topography of deformed shorelines, *Nature*, *447*(7146), 840–843, doi:10.1038/nature05873.
Phillips, R. J., et al. (2001), Ancient geodynamics and global-scale hydrology on Mars, *Science*, *291*(5513), 2587–2591, doi:10.1126/science.1058701.
Platz, T., and G. Michael (2011), Eruption history of the Elysium Volcanic Province, Mars, *Earth Planet. Sci. Lett.*, *312*(1–2), 140–151, doi:10.1016/j.epsl.2011.10.001.
Quantin, C., J. Flahaut, H. Clenet, P. Allemand, and P. Thomas (2012), Composition and structures of the subsurface in the vicinity of Valles Marineris as revealed by central uplifts of impact craters, *Icarus*, *221*(1), 436–452, doi:10.1016/j.icarus.2012.07.031.
Rathbun, J. A., and S. W. Squyres (2002), Hydrothermal systems associated with Martian impact craters, *Icarus*, *157*(2), 362–372, doi:10.1006/icar.2002.6838.
Rice, M. S., E. A. Cloutis, J. F. Bell, D. L. Bish, B. H. Horgan, S. A. Mertzman, M. A. Craig, R. W. Renaut, B. Gautason, and B. Mountain (2013), Reflectance spectra diversity of silica-rich materials: Sensitivity to environment and implications for detections on Mars, *Icarus*, *223*(1), 499–533, doi:10.1016/j.icarus.2012.09.021.
Roach, L. H., J. F. Mustard, G. Swayze, R. E. Milliken, J. L. Bishop, S. L. Murchie, and K. Lichtenberg (2010), Hydrated mineral stratigraphy of Ius Chasma, Valles Marineris, *Icarus*, *206*(1), 253–268, doi:10.1016/j.icarus.2009.09.003.
Robbins, S. J., and B. M. Hynek (2012), A new global database of Mars impact craters ≥1 km: 1. Database creation, properties, and parameters, *J. Geophys. Res.*, *117*, E05004, doi:10.1029/2011JE003966.
Ruff, S. W., and P. R. Christensen (2002), Bright and dark regions on Mars: Particle size and mineralogical characteristics based on thermal emission spectrometer data, *J. Geophys. Res.*, *107*(E12), 5127, doi:10.1029/2001JE001580.

Salvatore, M. R., and P. R. Christensen (2014a), Evidence for widespread aqueous sedimentation in the northern plains of Mars, *Geology*, *42*(5), 423–426, doi:10.1130/G35319.1.
Salvatore, M. R., and P. R. Christensen (2014b), On the origin of the Vastitas Borealis Formation in Chryse and Acidalia Planitiae, Mars, *J. Geophys. Res. Planets*, *119*, 2437–2456, doi:10.1002/2014JE004682.
Salvatore, M. R., J. F. Mustard, M. B. Wyatt, and S. L. Murchie (2010), Definitive evidence of Hesperian basalt in Acidalia and Chryse Planitiae, *J. Geophys. Res.*, *115*, E07005, doi:10.1029/2009JE003519.
Schwenzer, S. P., et al. (2012), Puncturing Mars: How impact craters interact with the Martian cryosphere, *Earth Planet. Sci. Lett.*, *335–336*, 9–17, doi:10.1016/j.epsl.2012.04.031.
Skinner, J. A., Jr., K. L. Tanaka, and T. Platz (2012), Widespread loess-like deposit in the Martian northern lowlands identifies middle Amazonian climate change, *Geology*, *40*, 1127–1130, doi:10.1130/G33513.1.
Smith, D. E., et al. (1999), The global topography of Mars and implications for surface evolution, *Science*, *284*(1495), 1495–1503, doi:10.1126/science.284.5419.1495.
Smith, M. R., J. L. Bandfield, E. A. Cloutis, and M. S. Rice (2013), Hydrated silica on Mars: Combined analysis with near-infrared and thermal-infrared spectroscopy, *Icarus*, *223*(2), 633–648, doi:10.1016/j.icarus.2013.01.024.
Sun, V. Z., and R. E. Milliken (2015), Ancient and recent clay formation on Mars as revealed from a global survey of hydrous minerals in crater central peaks, *J. Geophys. Res. Planets*, *120*, 2293–2332, doi:10.1002/2015JE004918.
Sunshine, J. M., and C. M. Pieters (1998), Determining the composition of olivine from reflectance spectroscopy, *J. Geophys. Res.*, *103*(E6), 13,675–13,688.
Tanaka, K. L. (1997), Sedimentary history and mass flow structures of Chryse and Acidalia Planitiae, Mars, *J. Geophys. Res.*, *102*, 4131–4149, doi:10.1029/96JE02862.
Tanaka, K. L., and D. H. Scott (1987), Geologic map of the polar regions of Mars, U.S. Geol. Surv. MiSci. Invest. Ser., Map I-1802-C, scale 1:15,000,000.
Tanaka, K. L., W. B. Banerdt, J. S. Kargel, and N. Hoffman (2001), Huge, CO_2-charged debris-flow deposit and tectonic sagging in the northern plains of Mars, *Geology*, *29*(5), 427–430, doi:10.1130/0091-7613(2001)029<0427:HCCDFD>2.0.CO;2.
Tanaka, K. L., J. A. Skinner Jr., T. M. Hare, T. Joyal, and A. Wenker (2003), Resurfacing history of the northern plains of Mars based on geologic mapping of Mars Global Surveyor data, *J. Geophys. Res.*, *108*, 8043, doi:10.1029/2002JE001908.
Tanaka, K. L., et al. (2005), Geologic map of the northern plains of Mars, U.S. Geol. Surv. Sci. Invest. Map, 2888.
Tanaka, K. L., J. A. P. Rodriguez, J. A. Skinner, M. C. Bourke, C. M. Fortezzo, K. E. Herkenhoff, E. J. Kolb, and C. H. Okubo (2008), North polar region of Mars: Advances in stratigraphy, structure, and erosional modification, *Icarus*, *196*(2), 318–358, doi:10.1016/j.icarus.2008.01.021.
Tanaka, K. L., C. M. Fortezzo, R. K. Hayward, J. A. P. Rodriguez, and J. A. Skinner (2011), History of plains resurfacing in the Scandia region of Mars, *Planet Space Sci.*, *59*(11–12), 1128–1142, doi:10.1016/j.pss.2010.11.004.
Tanaka, K. L., S. J. Robbins, C. M. Fortezzo, J. A. Skinner, and T. M. Hare (2014), The digital global geologic map of Mars: Chronostratigraphic ages, topographic and crater morphologic characteristics, and updated resurfacing history, *Planet. Space Sci.*, *95*, 11–24.
Tornabene, L. L., J. E. Moersch, H. Y. McSween, V. E. Hamilton, J. L. Piatek, and P. R. Christensen (2008), Surface and crater-exposed lithologic units of the Isidis based as mapped by coanalysis of THEMIS and TES derived data products, *J. Geophys. Res.*, *113*, E10001, doi:10.1029/2007JE002988.
Tosca, N. J., and A. H. Knoll (2009), Juvenile chemical sediments and the long term persistence of water at the surface of Mars, *Earth Planet. Sci. Lett.*, *286*(3–4), 379–386, doi:10.1016/j.epsl.2009.07.004.
Velde, B. (1985), *Clay Minerals: A Physico-Chemical Explanation of Their Occurrence*, *Dev. Sedimentol*, vol. 40, 427 pp., Elsevier, New York.
Viviano-Beck, C. E., et al. (2014), Revised CRISM spectral parameters and summary products based on the currently detected mineral diversity on Mars, *J. Geophys. Res. Planets*, *119*, 1403–1431, doi:10.1002/2014JE004627.
Weaver, C. E. (1989), *Clays, Muds, and Shales*, vol. 44, Elsevier, New York.
Wyatt, M. B., and H. Y. McSween (2002), Spectral evidence for weathered basalt as an alternative to andesite in the northern lowlands of Mars, *Nature*, *417*(6886), 263–266, doi:10.1038/417263a.
Yoshikawa, K. (2003), Origin of the polygons and the thickness of Vastitas Borealis Formation in Western Utopia Planitia on Mars, *Geophys. Res. Lett.*, *30*(12), 1603, doi:10.1029/2003GL017165.
Zhong, S. J., and M. T. Zuber (2001), Degree-1 mantle convection and the crustal dichotomy on Mars, *Earth Planet. Sci. Lett.*, *189*(1–2), 75–84, doi:10.1016/S0012-821x(01)00345-4.
Zuber, M. T., et al. (2000), Internal structure and early thermal evolution of Mars from Mars Global Surveyor topography and gravity, *Science*, *287*(5459), 1788–1793, doi:10.1126/science.287.5459.1788.

Erratum

In the originally published version of this paper, a Mann-Whitney U-test was used to estimate the statistical significance of the mineral detections in each geological basin in Section 4.3.2. Fisher's exact test and chi-square test, were then performed for the mafic and hydrated detections in each geological basin (Table 1). The overall trends remain the same, but the p-value of the significance varies slightly. In particular, hydrated mineral detections within Chryse Planitia, and Lyot vicinity are statistically distinct at the 90% confidence level in both Fisher's exact test and chi-square test, in comparison to the 95% confidence level in Mann-Whitney U test. Mafic mineral detections in Arcadia, Chryse and Utopia are statistically distinct at the 95% confidence level in all tests.

Additionally, in both Table 1 and Figure 14b of the original paper, the total number of craters in Utopia Planitia should be "n=229". In Figure 7, the mineral occurrences of olivine and pyroxene should be 585 and 139 respectively. In Section 4.1, the text should read "In total, 251 craters (~24%) are found with 724 occurrences of mafic minerals." In Section 4.2.1, the text should read "Mafic minerals are widespread in 24% of craters of different sizes, including 585 occurrences of olivine in 246 craters and 139 occurrences of pyroxene in 69 craters (Figure 7)." In the Supplementary Dataset, the missing detection of CRISM image HRL00023834 should be olivine and pyroxene detected on the central peak, and the missing coordinates of image FRS0002FE65 should be (3.168N, 161.640E).

This version has since been updated to reflect these changes and may be considered the version of record.